CCDC66 Controls Mitotic Progression and Cytokinesis by Promoting Centrosome Maturation and Microtubule Bundling

by

Umut Batman

A Dissertation Submitted to the
Graduate School of Sciences and Engineering
in Partial Fulfillment of the Requirements for
the Degree of

Master of Science

in

Molecular Biology and Genetics

September, 2021

CCDC66 Controls Mitotic Progression and Cytokinesis by Promoting Centrosome Maturation and Microtubule Bundling

Koç University

Graduate School of Sciences and Engineering

This is to certify that I have examined this copy of a master's thesis by

Umut Batman

and have found that it is complete and satisfactory in all respects,

and that any and all revisions required by the final

examining committee have been made.

Committee Members:

Assoc. Prof. Elif Nur Fırat Karalar (Advisor, Koç University)

Prof. Dr. Arzu Çelik (Boğaziçi University)

Assist. Prof. Ece Öztürk (Koç University)

September 2021

To my family and friends for their endless love and support…

ABSTRACT

Precise spatiotemporal control of microtubule nucleation and organization during mitosis and cytokinesis is critical for faithful segregation of cytoplasmic and genetic material. Microtubule-associated proteins (MAPs) govern the assembly, maintenance, and remodelling of microtubule arrays of cell division. Their deregulation causes cancer and developmental disorders. Despite having a nearly complete list of mitotic and cytokinetic MAPs, key questions remain about their functions and mechanisms, their regulation in different contexts and the nature of their crosstalk with different cellular structures. In this study, we identified the centrosomal and ciliary MAP, CCDC66, as a component of the bipolar spindle, central spindle and midbody. CCDC66 regulates mitotic microtubule nucleation via centrosomal recruitment of CDK5RAP2, Pericentrin and gamma-tubulin. Accordingly, CCDC66-depleted cells have defective spindle assembly, organization, and positioning, unstable K-fibers and chromosome alignment defects. Phenotypic rescue experiments revealed that its microtubule and centrosome pools mediate its mitotic functions. Furthermore, CCDC66 bundles microtubules in vitro and governs cytokinesis by regulating organization of the central spindle and midbody microtubule arrays. Our findings identify CCDC66 as a multifaceted regulator of cell cycle progression and advances our understanding of how nucleation and organization of distinct microtubule arrays are regulated.

ÖZETÇE

Mitoz ve sitokinez sırasında mikrotübül çekirdeklenmesinin ve organizasyonunun tam uzay-zamansal kontrolü, sitoplazmik ve genetik materyalin güvenilir bir şekilde ayrılması için kritik öneme sahiptir. Mikrotübül ilişkili proteinler (MAP'ler), hücre bölünmesinin mikrotübül dizilerinin birleştirilmesini, bakımını ve yeniden modellenmesini yönetir. Deregülasyonları kansere ve gelişimsel bozukluklara neden olur. Mitotik ve sitokinetik MAP'lerin listesinin neredeyse eksiksiz olmasına rağmen, işlevleri ve mekanizmaları, farklı bağlamlardaki düzenlemeleri ve farklı hücresel yapılarla karışmalarının doğası hakkında temel sorular devam etmektedir. Bu çalışmada, bipolar iğ, merkezi iğ ve iğ kalıntısının bir bileşeni olarak CCDC66'yı sentrozomal ve siliyer MAP olarak tanımladık. CCDC66'nın, CDK5RAP2, Pericentrin ve gama-tubulinin sentrozomal alımı yoluyla mitotik mikrotübül çekirdeklenmesini düzenlendiğini gösterdik. Buna göre, CCDC66-tükenmiş hücreler, hatalı iğ montajı, organizasyonu ve konumlandırması, kararsız K-lifleri ve kromozom hizalama kusurlarına sahiptir. Fenotipik kurtarma deneyleri, mikrotübül ve sentrozom havuzlarının mitotik işlevlerine aracılık ettiğini ortaya çıkardı. Ayrıca, CCDC66 mikrotübülleri in vitro demetleyerek ve merkezi iğ ve iğ kalıntısı mikrotübül dizilerinin organizasyonunu düzenleyerek sitokinezi yönetir. Bulgularımız CCDC66'yı hücre döngüsü ilerlemesinin çok yönlü bir düzenleyicisi olarak tanımlar ve farklı mikrotübül dizilerinin çekirdeklenmesinin ve organizasyonunun nasıl düzenlendiğine dair anlayışımızı ilerletir.

AKNOWLEDGEMENTS

I would like to acknowledge my supervisor Dr. Elif Nur Fırat-Karalar for her invaluable help and support during my studies. Her passion and ambition for science motivated me to become a better scientist. It was truly a privilege to be a member of Cytoskeleton Research Lab.

Next, I would like to thank my thesis committee members Dr. Ece Öztürk and Prof. Dr. Arzu Çelik Fuss for their valuable comments and insights regarding my thesis work.

My biggest thanks go to my dearest family; my mother Vehibe, my father Ali, my sister İnci and my brother Teysir, without whom I would not be who I am today. It was not the easiest childhood or teenage years going through really difficult times, but we hold onto each other. Looking back, we may not have had much but your endless love and support was more than we can ask for. I love you all.

I would like to thank Fatmanur Tiryaki for being my other half. We have been inseparable for the past three years as home mates and lab mates and spent almost 7/24 together. We had all the joyful and stressful times and survived together. I am looking forward to having new memories in the next phase of our lives. I would like to thank the other member of our sweet home Ezgi Memiş for being an amazing friend. Even though we are separated by oceans now, I know that it never truly separates us. I would like to thank Çağla Çakmak for always understanding and thinking of me. I feel lucky to be your friend and cannot wait to reunite with you again. I would like to thank Feyza Arzu and Aysun Acar for being my second family. I cannot express my love for you and cannot think of my life without you. I would like to thank the minis Özge Osmanoğlu, Ezgi Osmanoğlu and Suat Dönertaş for always being there for me. We always have the fun and craziest moments together.

I would like to acknowledge the members and alumni of Fırat-Karalar Lab. Deniz Çonkar and Jovana Deretic, thank you for always helping me when I needed it. You inspired me to become better. I will always look up to you. I would like to thank Ezgi Odabaşı and Melis Dilara Arslanhan. I will miss your loud laughters and energy. I would like to thank Ebru Topçu and Dila Gülensoy for the amazing times and out lab activities we did together. We spent so many hours in animal facility with Ebru, I will miss our little weird moments and impressions. I would like to thank Başak Turan, Erdem Ercan and Efe Begar for being so considerate and helpful. I will miss messing with you.

Finally, I would like to acknowledge the financial support for this study from Tübitak projects entitled as; TUBITAK BIDEB 120C148 Primer Silyum, Silyopatiler ve Mikrotübül-ilişkili Proteinler arasındaki moleküler ve fonksiyonel ilişkinin belirlenmesi to “Elif Nur Firat Karalar” and TUBITAK ARDEB 120Z179 Primer Siliyer Oluşumunun ve Fonksiyonlarının Moleküler Temellerinin Tanımlanması to “Jovana Deretic”.

TABLE OF CONTENTS

LIST OF FIGURES

ABBREVIATIONS

α-Tubulin	Alpha Tubulin
ATCC	American Type Culture Collection
BIRA*	Promiscuous Biotin Protein Ligase
BioID	Proximity-Dependent Biotin Identification
BSA	Bovine Serum Albumin
CCDC66	Coiled-coil domain containing protein 66
CDK5RAP2	CDK5 regulatory subunit-associated protein 2
Cep55	Centrosomal Protein of 55 kDa
Cep152	Centrosomal Protein of 152 kDa
Cep192	Centrosomal Protein of 192 kDa
Cep290	Centrosomal Protein of 290 kDa
CPC	Chromosomal Passenger Complex
CSPP1	Centrosome and Spindle Pole-Associated Protein 1
DAPI	4’,6-diaminodino-2-phenylindole
DMEM	Dulbecco’s Modified Eagle Medium
DMEM/F12	DMEM/Nutrient Mixture-12
DMSO	Dimethyl sulfoxide
DNA	Deoxyribonucleic Acid
EB1	End Binding 1
EGTA	Ethylene glycol-bis(2-aminoethylether)-N,N,N’
FBS	Fetal Bovine Serum
G0	Gap0
G1	Gap1
G2	Gap2
GAPDH	Glyceraldehyde 3-Phosphate Dehydrogenase
GO	Gene Ontology
GFP	Green Fluorescence Protein
g-TURC	Gamma-Tubulin Ring Complex
IFT88	Intraflagellar Transport Protein 88
IP	Immunoprecipitation
K-Fiber	Kinetochore Fiber

MAP	Microtubule Associated Protein
MAP65	Microtubule Associated Protein 65
MBP	Maltose Binding Protein
MKLP1	Kinesin-like Protein Kif23
mNG	mNeon-Green
MT	Microtubule
MTOC	Microtubule Organizing Center
PBS	Phosphate-buffered saline
PCM	Pericentriolar Material
PCM1	Pericentriolar Material 1
PCNT	Pericentrin
PEI	Polyethylenimine
pH3	Phosphorylated Histone 3
PLK1	Polo-like Kinase 1
PRC1	Protein Regulator of Cytokinesis 1
RanGTP	GTP-binding Nuclear Protein Ran
RD	Retinal Degeneration
RNA	Ribonucleic Acid
RPE1 hTERT	telomerase immortalized retinal pigment epithelial cells
SiRNA	Short Interfering RNA
SDS-PAGE	Sodium Dodecyl Sulfate-Polyacrylamide Gel Electrophoresis
STLC	S-trityl-Lcysteine
TBST	Tris-Buffered Saline, 0.1% Tween®
TOGARAM1	TOG array regulator of axonemal microtubules protein 1
U-ExM	Ultrastructure Expansion Microscopy
U2OS	human osteosarcoma cells
γ-Tubulin	Gamma Tubulin

Chapter 1:
INTRODUCTION

Faithful segregation of genetic and cytoplasmic material during cell division is essential for growth and development of multicellular organisms. Deregulation of the molecular processes regulating cell division leads to aneuploidy and chromosomal instability and thereby to the initiation and progression of various human cancers. As such, mitosis and cytokinesis are highly regulated, multistep processes involving dynamic regulation and coordinated activity of multiple cellular structures and signaling pathways. In particular, microtubule cytoskeleton undergoes a series of morphological changes to ensure the fidelity of cell division. First, microtubules assemble the bipolar spindle, which captures, aligns and segregates the duplicated chromosomes to daughter cells. During early anaphase, antiparallel non-kinetochore microtubules are bundled at their plus ends to form the central spindle between separating sister chromatids. The plus ends of the central spindle microtubules overlap at the spindle midzone, which compacts into the midbody upon cleavage furrow ingression. Central spindle, spindle midzone and midbody are required for keeping sister chromosomes apart, positioning the cleavage furrow and completion of cytokinesis. Given their crucial roles during chromosome segregation, deregulation of the diverse microtubule arrays of dividing cells leads to aneuploidy and chromosomal instability and thereby to the initiation and progression of various human cancers.

Precise spatiotemporal control of the assembly, maintenance and dynamic remodeling of the mitotic spindle and central spindle is critical for proper progression through mitosis and cytokinesis. The dynamics, organization and stability of these microtubule arrays requires a diverse group of proteins including microtubule-associated proteins (MAPs), cellular structures and signaling pathways. MAPs, which include molecular motors and non-motor proteins, bind to microtubules and regulate their dynamic properties, organization and stability as well as their interactions with other proteins and cellular structures (Maiato et al., 2004; Petry, 2016). Proteomic profiling of microtubule-based structures of dividing cells, functional screens and loss-of-function studies have identified hundreds of MAPs as regulators of mitosis and cytokinesis (Amin et al., 2019; Petry, 2016). Individual characterization of a group of these MAPs revealed their functions in the formation of the mitotic spindle and central spindle,

chromosome capture and segregation, cleavage furrow formation and abscission. Despite the progress made towards identification of the mitotic and cytokinetic MAPs, key questions remain about their functions and mechanisms, as well as how they cooperate with different cellular structures, upstream and downstream factors to modulate the microtubule parameters that ultimately define the size, shape, and dynamics of microtubule arrays. Additionally, given that the mitotic spindle and central spindle are both bipolar microtubule arrays, whether and to what extent the mechanisms, in particular the MAPs, underlying their assembly and maintenance are shared and distinct is not well understood. Addressing these questions will provide insight into the mechanisms by which microtubules undergo dramatic changes to carry out their essential functions during cell division.

1.1 Centrosome Maturation & Microtubule Nucleation

Microtubule nucleation, bundling and stabilization are among the essential activities exerted by MAPs during mitosis and cytokinesis. In animal somatic cells, microtubule nucleation is initiated at multiple locations, including the centrosomes, preexisting spindle microtubules and chromatin (Duncan and Wakefield, 2011; Petry and Vale, 2015) (Figure1). The mechanisms by which these distinct pathways work, and the extent of their crosstalk have been an area of active investigation.

Microtubules in all eukaryotic cells are composed of α/β tubulin dimers which assemble 25 nm hollow cylindrical filaments. Tubulin dimers both *in cell* and *in vitro* can assemble when their concentration exceeds 'critical concentration', however; this spontaneous nucleation is not efficient and in cells, they require other factors to start the nucleation. The best characterized pathway for microtubule nucleation is the gamma-tubulin ring complex (γ-TURC) which is associated with several other protein complexes named γ-tubulin complex proteins (GCP). GCPs directly or indirectly binds to γ-tubulin to activate and increase the nucleation efficiency of γ-TURC which binds to α tubulin to template the growth of microtubules from the minus end.

Dynamic instability is characteristic feature of microtubules, which defines the constant state of elongation and shrinkage of microtubules mostly from their plus ends. Upon nucleation, microtubule plus end binding proteins such as EB1 and XMAP215 stabilizes plus ends and accelerate the growth of the microtubules while katanin and kinesin-13 induces catastrophe by

severing or disassembling the microtubules. Other MAPs like Tau protein in neuronal cells, binds to microtubules on lateral surface and protect them from catastrophe by stabilization.

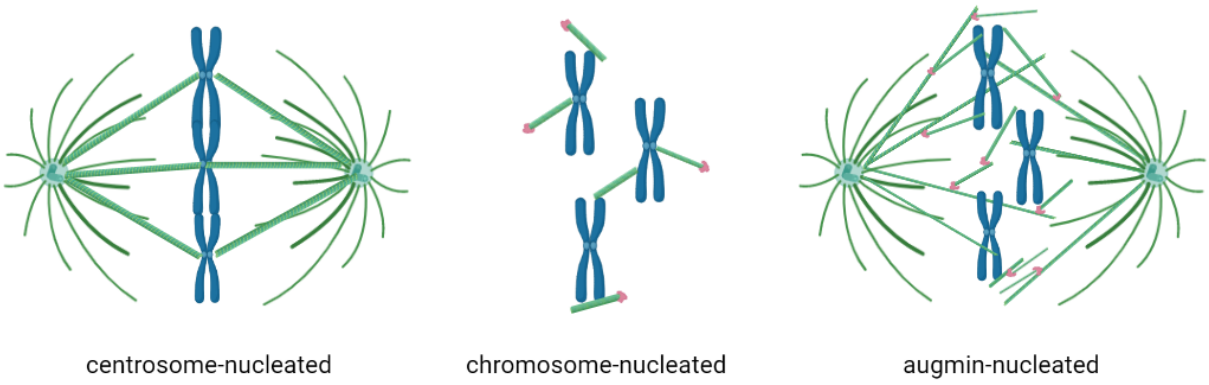

Figure 1. Microtubule nucleation pathways during mitosis (adapted from biorender)

Centrosomes are the major microtubule-organizing centers in dividing cells. They are composed of two centrioles and associated pericentriolar material (PCM) that contains the proteins required for microtubule nucleation such as the gamma-tubulin ring complex (g-TURC). As cells enter mitosis, PCM expands in a process called centrosome maturation, which increases its microtubule-nucleation capacity (Palazzo et al., 2000). (Figure 2) Centrosome maturation is initiated by PLK1-dependent phosphorylation of Pericentrin and CDK5RAP2, which promotes recruitment of additional PCM proteins including Cep152, Cep192 and gamma-tubulin (Cabral et al., 2019; Choi et al., 2010; Conduit et al., 2014; Dobbelaere et al., 2008; Gomez-Ferreria et al., 2007; Hanafusa et al., 2015; Joukov et al., 2014; Lee and Rhee, 2011). Cep152 is a dual regulator of centriole duplication and centrosome maturation. It spans the PCM by its C-terminal part being close to the centriole wall and its N-terminal part extending towards the PCM ring so that it can function during assembly of the PCM. Cep192 is a crucial component of PCM as it scaffolds both PLK1 and Aurora-A kinase to target them to centrosomes which in turn phosphorylates downstream components to expand centrosomes. Pericentrin, like Cep152, also laterally spans the PCM determining the size of the PCM in interphase cells. Pericentrin also creates binding sites for Cdk5Rap2 with binds to gamma-tubulin and activates γ-TURC.

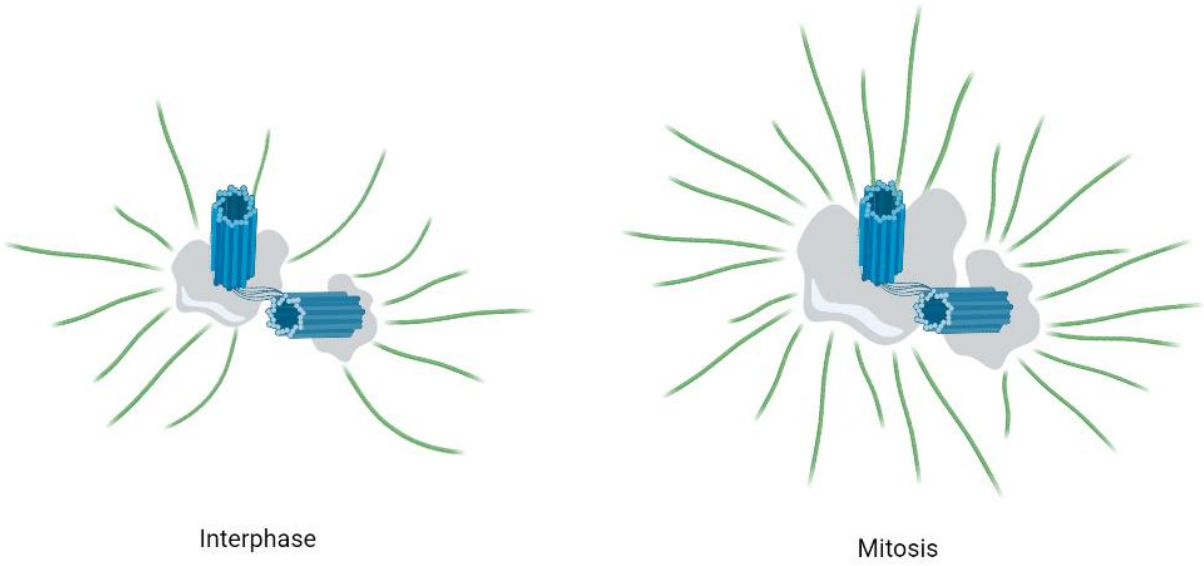

Figure 2. Centrosome Expansion and Increase in MT Nucleation Capacity (adapted from biorender)

Acentrosomal microtubule nucleation during mitosis is triggered at the chromosomes in RanGTP, Op8/Stathmin and the chromosomal passenger complex (CPC)-dependent pathways, and at the spindle microtubules in a HAUS/augmin complex-dependent way (Goshima et al., 2008; Goshima et al., 2007; Heald et al., 1996; Petry and Vale, 2015). HAUS complex is composed of 8 proteins namely HAUS1, 2, 3, 4, 5, 6, 7, and HAUS8. HAUS1-HAUS8 forms a hetero-octameric complex with a 40 nm extended Y shape. In mitotic cells, gamma TURC complex is found on the spindle microtubules. The previous studies showed that the depletion of gamma tubulin from the spindle microtubules reduced the amount of the microtubules. In the complex, HAUS8 directly binds to microtubules while HAUS6 binds NEDD1 which recruits gamma tubulin. Thereby, HAUS6 connects the gamma TURC complex to the microtubules allowing branching microtubule formation on a daughter microtubule.

1.2 K-Fibers and Microtubule Bundling

Organization of MTs into highly ordered mitotic and cytokinetic arrays play critical roles for cell division. For example, 20-40 kinetochore MTs in human cells form parallel bundles termed K-fibers, which run from spindle poles to kinetochores and are essential for chromosome alignment and segregation (Booth et al., 2011; McDonald et al., 1992; McEwen et al., 1997; Tolic, 2018). Bridging fibers, composed of antiparallel bundles of interpolar MTs,

connect two sister K-fibers and push them apart to separate spindle poles (Tolic, 2018; Vukusic et al., 2017). Similarly, in anaphase, an antiparallel MT bundle forms the central spindle/midzone which pushes the spindle poles to opposite side of the cell and directs the localization of ingression furrow important for the division of cytoplasm (Glotzer, 2009). Anti-parallel MT bundles at the spindle midzone are crosslinked by the evolutionarily conserved PRC1/Ase1/MAP65 family (Bieling et al., 2010; Janson et al., 2007; Mollinari et al., 2002; Subramanian et al., 2010). (Figure 3) Central spindle shortens to form the midbody during cytokinesis, which will direct the membrane abscission site (Hu et al., 2012). Moreover, astral MTs, which emanate from the centrosomes, interact with the cell cortex to position the spindle within a cell and determine the initial cleavage plane through communication with the equatorial cortex (D'Avino et al., 2005). Although multiple MAPs involved in the formation and stabilization of the distinct spindle bundles have been identified, the full extent of MAPs involved in MT crosslinking and stability as well as their mechanism of action have yet to be determined in future studies.

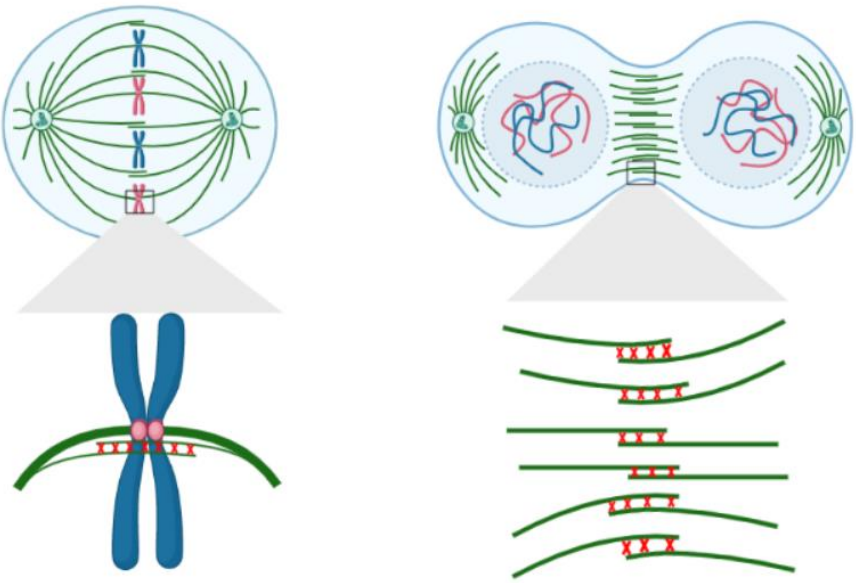

Figure 3. Microtubule Bundling During Mitosis (adapted from biorender)

1.3 MAPs with Dual Roles in Cell Cycle

Changes from the interphase MT network to the described MT organization and dynamics in cell division are drastic. They require precise regulation of when and where MAPs are activated during cell cycle. A subset of MAPs is active during mitosis but inactive during interphase. Such regulation is achieved by modulation of their affinity to MTs, regulation of their cellular abundance and localization and posttranslational modifications (Syred et al.,

2013). Importantly, there is also a group of MAPs with dual functions in dividing and non-dividing cells (Akhmanova et al., 2001; Akhmanova and Steinmetz, 2015; Kaplan et al., 2001; Villari et al., 2020). For example, End Binding 1 (EB1) regulates MT plus-end dynamic and targets other MAPs to the plus ends both in interphase and mitosis. Recently, a critical regulator of primary cilium assembly in nondividing cells, Intraflagellar transport Protein 88 (IFT88), has been described for its functions during mitotic spindle orientation and central spindle organization (Delaval et al., 2011; Taulet et al., 2019). Importantly, the discovery of non-ciliary functions of IFT88 unraveled that its mutations might contribute to polycystic kidneys with both impaired ciliary function and aberrant cell division (Delaval et al., 2011; Taulet et al., 2019). Despite the progress made in the characterization of MAPs with dual roles in cycling and non-cycling cells, questions remain about their functions, mechanisms, and modes of regulation in different stages of the cell cycle.

1.4 CCDC66

We previously characterized coiled coil protein 66 (CCDC66) as a MAP and as a regulator of primary cilium formation and composition in quiescent cells. CCDC66 dynamically localizes to the centrosome, centriolar satellites, primary cilium and MTs in different cell states (Conkar et al., 2019; Conkar et al., 2017). It was originally described as a gene mutated in retinal degeneration and later characterized for its retinal and olfactory functions using CCDC66-/- mouse (Dekomien et al., 2010; Gerding et al., 2011; Murgiano et al., 2020; Schreiber et al., 2018). Recently, CCDC66 was identified as part of the Joubert syndrome interaction network consisting of other MAPs such as CSPP1, TOGARAM1 and CEP290 (Latour et al., 2020). Consistent with its link to ciliopathies, we and others previously showed that retinal degeneration mutations disrupt its ciliary functions and interactions (Conkar et al., 2017; Murgiano et al., 2020). In addition to its functions at the primary cilium, following lines of evidence suggest that CCDC66 might function as a MAP and centrosome protein that regulates cell division: CCDC66 mRNA was identified in the MT-interacting transcriptome of Xenopus tropicalis, indicative of its functions during MT-based cellular processes (Sharp et al., 2011). Additionally, CCDC66 localized to spindle poles and MTs and its depletion led to disorganized poles in mitotic cells (Conkar et al., 2017; Sharp et al., 2011). Finally, CCDC66 proximity interactome generated from asynchronous HEK293T cells revealed interactions with regulators of cell division (Conkar et al., 2017; Gheiratmand et al., 2019; Gupta et al., 2015). The full extent of CCDC66 functions during different stages of cell division and the underlying

molecular mechanisms are not known. Addressing these key unknowns will uncover the relationship of CCDC66 with other components of the mitotic and cytokinetic machinery and will also provide insight into whether and if so, how its nonciliary functions contribute to its disease mechanisms.

In this study, we examined the localization, interactions, functions, and mechanisms of CCDC66 during cell division. We showed that CCDC66 is required for recruitment of core PCM proteins to the spindle poles and acts as a bundling protein in vitro. Its association with centrosomes and MTs is required for spindle assembly and organization, k-fiber and midbody integrity, chromosome alignment, and cytokinesis. Our findings unravel non-ciliary functions for CCDC66 during cell division and provides insight into the integrated activity of centrosomes and MAPs during spatiotemporal regulation of MT nucleation and organization in dividing cells.

Chapter 2:
RESULTS

2.1 CCDC66 localizes to spindle poles and MTs during mitosis and cytokinesis

Based on its previously reported localization and interactions, we hypothesize that CCDC66 plays important roles during mitosis and cytokinesis (Conkar et al., 2017; Gheiratmand et al., 2019; Gupta et al., 2015; Sharp et al., 2011). To test this, we first examined localization of CCDC66 at different cell cycle stages in human osteosarcoma (U2OS) and telomerase immortalized retinal pigment epithelial (RPE1-hTERT) cells. The commercial rabbit and home-made rat polyclonal antibodies raised against different CCDC66 antigens (antigen#1: 898-948 a.a., antigen#2: 1-831 a.a, antigen#3: 570-948 a.a.) did not detect endogenous CCDC66 in immunofluorescence experiments. Therefore, we used lentiviral transduction to generate cell lines that stably express mNeonGreen (mNG)-CCDC66. Its expression size was validated by immunoblotting using mNG antibody and immunofluorescence using anti-CCDC66 antibody (Fig. 5A-C). mNG protein was chosen over GFP as the fluorescent tag due to its higher fluorescent intensity and stability (Shaner et al., 2013). mNG-CCDC66 localized to the centrosome and centriolar satellites in interphase cells (Fig. 4A, 5D). In dividing cells, CCDC66 localized to the spindle poles and multiple MT-based structures including the spindle MTs in prometaphase and metaphase, the central spindle in anaphase and the midbody in cytokinesis in both U2OS and RPE1 stable lines (Fig. 4A, 5D). CCDC66 localization to the astral MTs was apparent in RPE1::mNG-CCDC66 cells, likely due to their flattened morphology that allows better visualization of astral MTs (Fig. 5D). To determine the dynamic behavior of CCDC66 during cell division, we performed timelapse imaging of the stable cells incubated with SIR-tubulin, which marks MTs. In agreement with its localization in fixed cells, mNG-CCDC66 dynamically localized to the centrosome, centriolar satellites and MT-based structures during mitosis and cytokinesis (Fig. 4B, 5E).

Previously, we showed that CCDC66 binds to MTs in vitro and localizes to the interphase centrosomes via its C-terminal 570-948 residues (Conkar et al., 2017). Therefore, we tested whether this fragment recapitulates the localization of full length CCDC66 during cell division. Like mNG-CCDC66, mNG-CCDC66 (570-948) localized to the spindle poles, bipolar spindle, and central spindle during mitosis and midbody during cytokinesis upon transient and stable expression in cells (Fig. 4C). Its expression at the expected size was

validated by immunoblotting (Fig. 5B). When overexpressed, mNG-CCDC66 formed cytoplasmic aggregates that recruited gamma-tubulin, suggesting a putative interaction between them (Fig. 4D). To investigate the functional significance of this recruitment during MT nucleation, we performed MT regrowth experiments and found that they nucleated MTs 10 min after nocodazole washout (Fig. 4D). Together, these data indicate that the C-terminal 379 residues of CCDC66 is sufficient for its cellular localization to the centrosome and MTs in dividing cells.

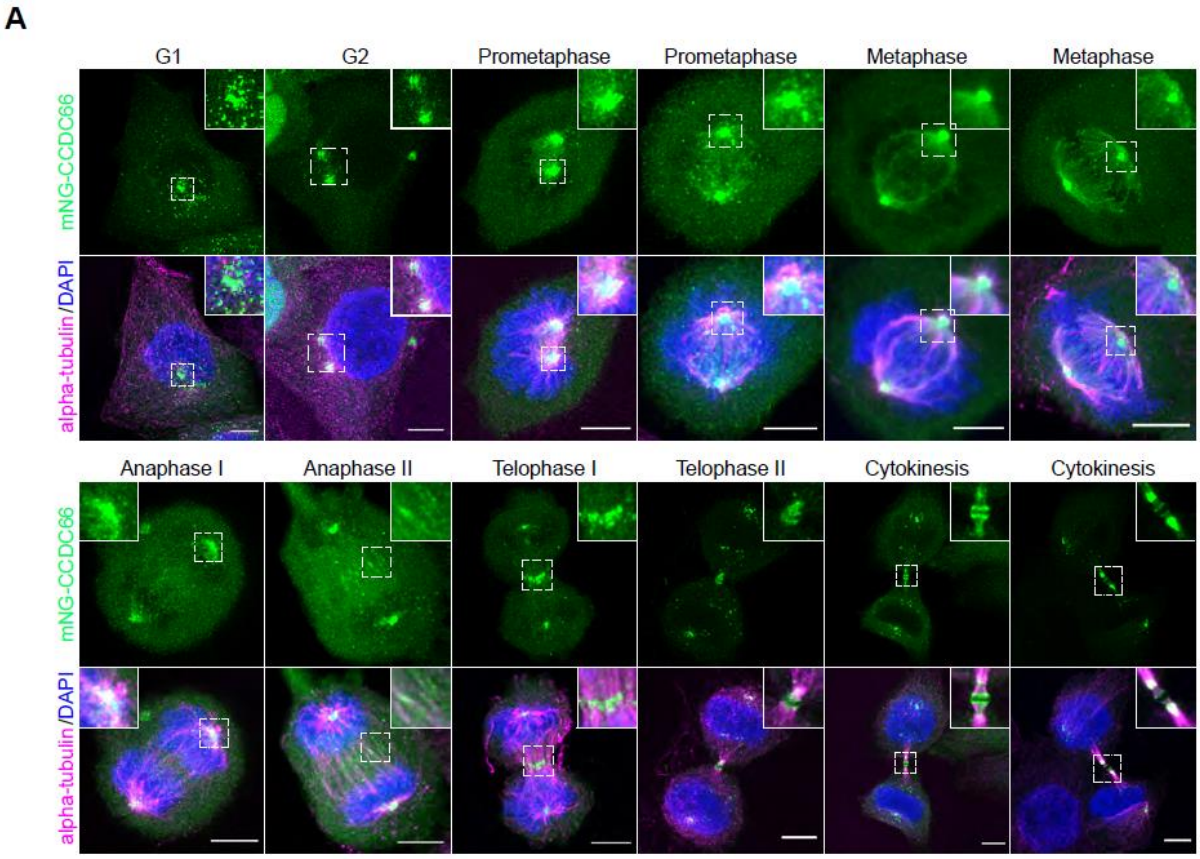

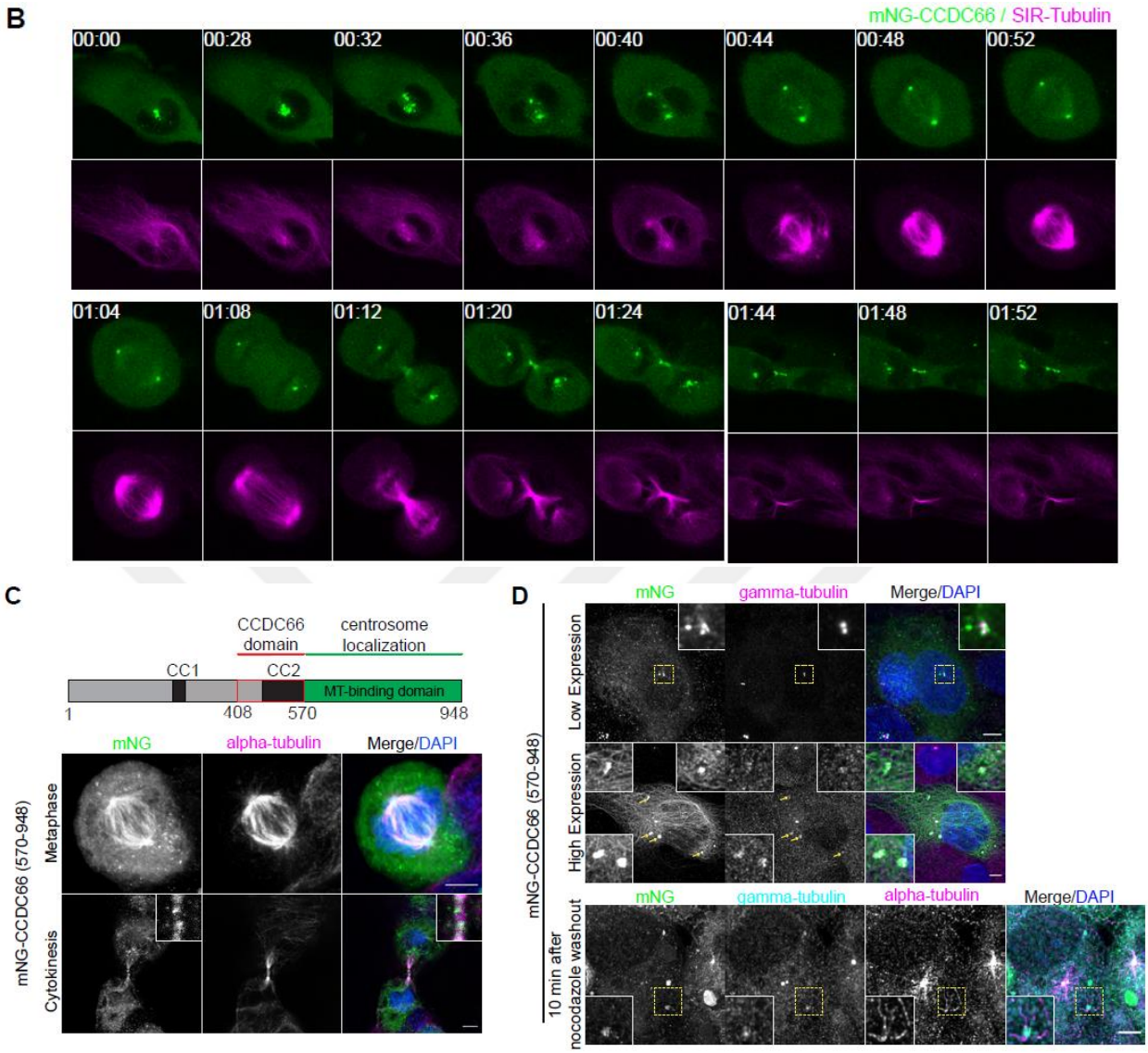

Figure 4. CCDC66 Localizes to microtubule-based structures during cell division.

(A) Localization of mNeonGreen-CCDC66 at different stages of the cell cycle. U2OS cells stably expressing mNeonGreen-CCDC66 fusion (U2OS::mNG-CCDC66) were fixed with 4% PFA and stained for alpha tubulin (α-Tubulin) and DAPI. Scale bar: 5 μm, insets show 4X magnifications of the boxed regions.

(B) Dynamic localization of mNeonGreen-CCDC66 throughout the cell cycle. U2OS cells stably expressing mNeonGreen-CCDC66 fusion (U2OS::mNG-CCDC66) were incubated with 100 nM SiR-Tubulin overnight. Images are acquired every 4 minutes using confocal microscopy. Shown are sixteen time-lapse images from Movie 1 at indicated time points to show dynamic localization of mNG-CCDC66 to spindle poles and microtubules during cell division.

(C) Schematic representation of full length (FL) CCDC66 domain organization. CC1 and CC2 indicate coiled-coil domains. The C-terminal region was previously described as a microtubule-binding region (Conkar et al., 2017). Still confocal images show U2OS cells transfected with mNeonGreen-CCDC66 C-terminal construct (mNG-CCDC66570-948). 24 h post-transfection, cells were fixed with 4% PFA and stained for α-tubulin and DAPI. mNG-CCDC66570-948 localizes to spindle poles and spindle microtubules during metaphase and to midbody during cytokinesis. Scale bar: 5 μm.

(D) mNG-CCDC66570-948 sequesters gamma-tubulin to cytoplasmic aggregates. U2OS cells were transfected with mNG-CCDC66570-948, fixed with 4% PFA and stained for γ- tubulin and DAPI. Top panel shows a lower expressing cell in which mNG-CCDC66570- 948 is restricted mostly to centrosomes. Middle panel shows a high-expressing cell with multiple cytoplasmic aggregates of mNG-CCDC66570-948 that co-localize with gammatubulin. Bottom panel shows mNG-CCDC66570-948 transfected cells that are treated with 5 μg/ml nocodazole for 1 h at 37 °C and incubated for 10 min after nocodazole washout. Scale bar: 5 μm, insets show 4X magnifications of the boxed regions.

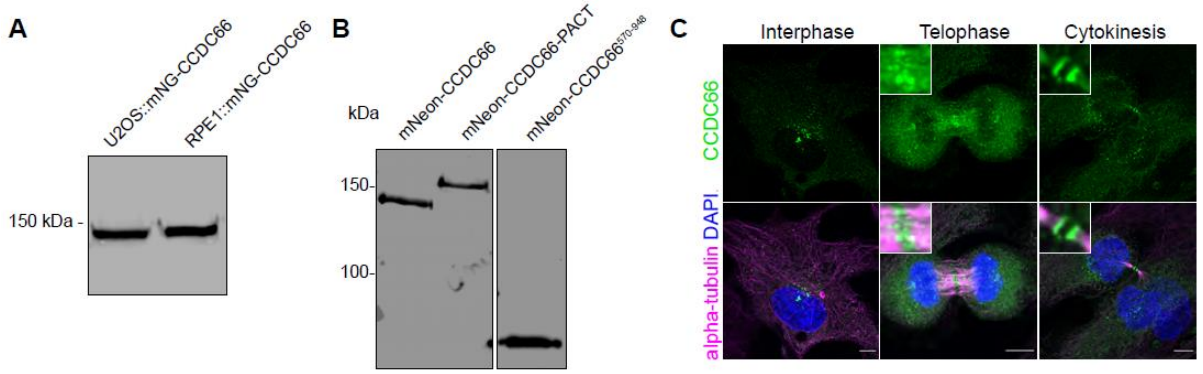

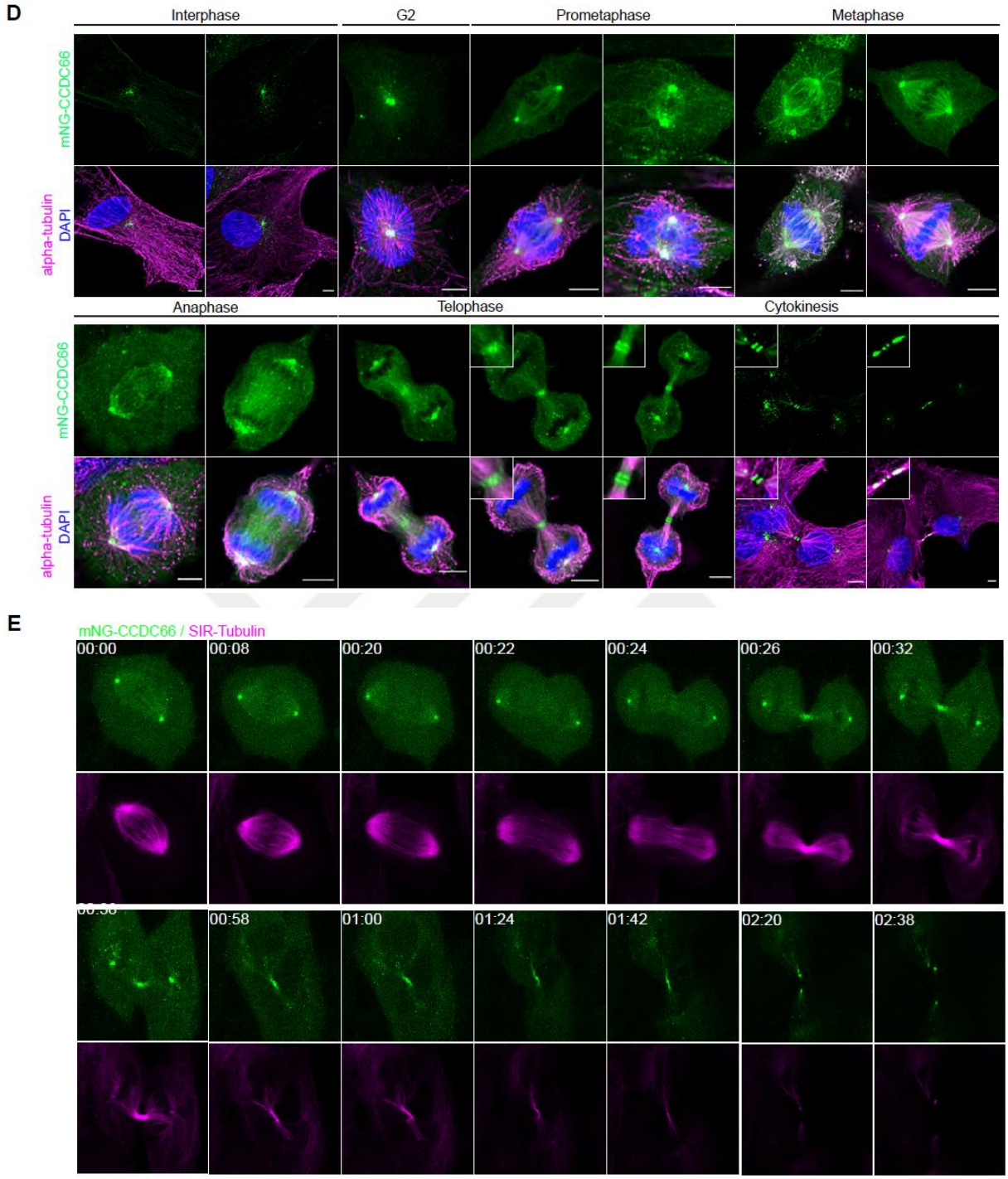

Figure 5. CCDC66 localization during cell cycle in RPE1 cells and validation of mNG-CCDC66-expressing cell lines

(A) Validation of mNG-CCDC66 expression in U2OS::mNG-CCDC66 and RPE1::mNGCCDC66 stable lines by immunoblotting. Extracts from cells were prepared, resolved by SDS-PAGE and blotted with mNG antibody.

(B) Validation of U2OS cells lines that stably express siRNA-resistant mNG-CCDC66, mNG-CCDC66-PACT and mNG-CCDC66 (570-948). Extracts from cells were prepared, resolved by SDS-PAGE and blotted with mNG antibody.

(C) Validation of RPE1::mNG-CCDC66 expression with antibody. RPE1::mNG-CCDC66 stable cell line was fixed with MeOH and stained with Rat CCDC66 antibody and alphatubulin. Insets show 4x zoom. Scale bar: 5 μm.

(D) Localization of mNeonGreen-CCDC66 at different stages of cell cycle. RPE1 cells stably expressing mNG-CCDC66 fusion (RPE1::mNG-CCDC66) were fixed with 4% PFA and stained for alpha-tubulin and DAPI. Scale bar: 5 μm.

(E) Dynamic localization of mNG-CCDC66 throughout the cell cycle. RPE1::mNGCCDC66 were incubated with 100 nM SiR-Tubulin overnight. Images were acquired every 2 minutes using confocal microscopy. Shown are fourteen time-lapse images from Movie S1 at the indicated time points.

2.2 CCDC66 co-localizes and interacts with critical regulators of mitosis and cytokinesis

We defined the high-resolution localization of CCDC66 at the mitotic and cytokinetic subcompartments reported in Fig. 4 relative to markers of the spindle poles, bipolar spindle, central spindle and midbody. To this end, we co-stained U2OS::mNG-CCDC66 cells with antibodies against PCM proteins gamma-tubulin, CEP192, CEP152, CDK5RAP2 (spindle poles), the MT-crosslinking protein PRC1 (central spindle and midbody MTs), the centrosome protein CEP55 (midbody core), the kinesin motor protein Kif23/MKLP1and phosphorylated Aurora A/B/C (midbody flanks) (Fry et al., 2017; Glotzer, 2009; Hu et al., 2012). CCDC66 localized to the spindle poles throughout mitosis, as shown by its co-localization with gamma-tubulin, CDK5RAP2, CEP192 and CEP152 (Fig. 6A, 6B). Like other PCM proteins, CCDC66 formed resolvable rings at the PCM (Fig. 6A, 6B). Notably, the spindle pole-associated pool of CCDC66 was maintained in nocodazole-treated cells, confirming that this pool binds to the spindle poles independent of MTs (Fig. 6C). To determine the precise cytokinetic localization of CCDC66, we performed plot profile analysis along the midbody MT bundles for CCDC66 and various midbody markers as described previously (Fig. 6D) (Hu et al., 2012). In cytokinesis, CCDC66 localized to two closely spaced bands at the midbody. Plot profile analysis revealed its co-localization with PRC1 at the dark zone (Fig. 6D), which is defined as the narrow region on the MT bundle in the center of the midbody (Hu et al., 2012). It did not co-localize with CEP55 and MKLP1, which are visualized as rings representing the bulge at the center of the

midbody, and phospho-Aurora (Fig. 6D), which marks the broader bands on MTs outside the dark zone (Hu et al., 2012).

To further generate hypothesis regarding the functions and mechanisms of CCDC66 during cell division, we compiled a list of CCDC66 interactors from high throughput proximity-mapping studies and performed Gene Ontology (GO)-enrichment analysis of its interactors. (Fig.7A, 7B) (Conkar et al., 2017; Gheiratmand et al., 2019; Gupta et al., 2015). In addition to the previously described functions related to the primary cilium, CCDC66 proximity interactors were enriched for biological processes related to cell division including spindle assembly and organization, chromosome segregation, metaphase plate congression and cytokinesis (Fig. 7A). Consistently, cellular compartments involved in these processes such as the HAUS complex, mitotic spindle, spindle pole and kinetochore were among the enriched GO categories (Fig.7B). This analysis suggests nonciliary functions for CCDC66 during different stages of cell division.

Next, we performed Flag-based co-immunoprecipitation experiments to define the physical mitotic and cytokinetic interactions of CCDC66. Specifically, we tested interactions with PCM proteins and mitotic MAPs that co-localizes with CCDC66 (Fig. 6A-D) or were previously described as critical regulators of mitosis and cytokinesis. As a positive control for interaction experiments, we used the centriolar satellite scaffolding protein PCM1, which we previously reported as an interactor for CCDC66 (Conkar et al., 2017). First, we assayed whether CCDC66 interacts with critical regulators of centrosome maturation. CCDC66 co-pelleted with myc-BirA* fusions of CDK5RAP2, Cep192, Cep152 and gamma-tubulin, but with the negative control myc-BirA* (Fig. 6E). CCDC66 also did not co-pellet with the MT plus-end-tracking protein EB1, confirming the specificity of its interactions with PCM proteins (Fig. 6E). Next, we tested its interactions with regulators of cytokinesis (Glotzer, 2009). Flag-BirA*-CCDC66 interacted with the GFP-PRC1, but not GFP-CEP55 and the negative control GFP (Fig. 6F). The new relationships revealed by the immunoprecipitation experiments are in agreement with the co-localization of CCDC66 with the spindle pole and midbody proteins (Fig. 6A-D). Taken together, our results suggest that CCDC66 functions during mitosis and cytokinesis by regulating centrosome maturation, MT nucleation and/or organization.

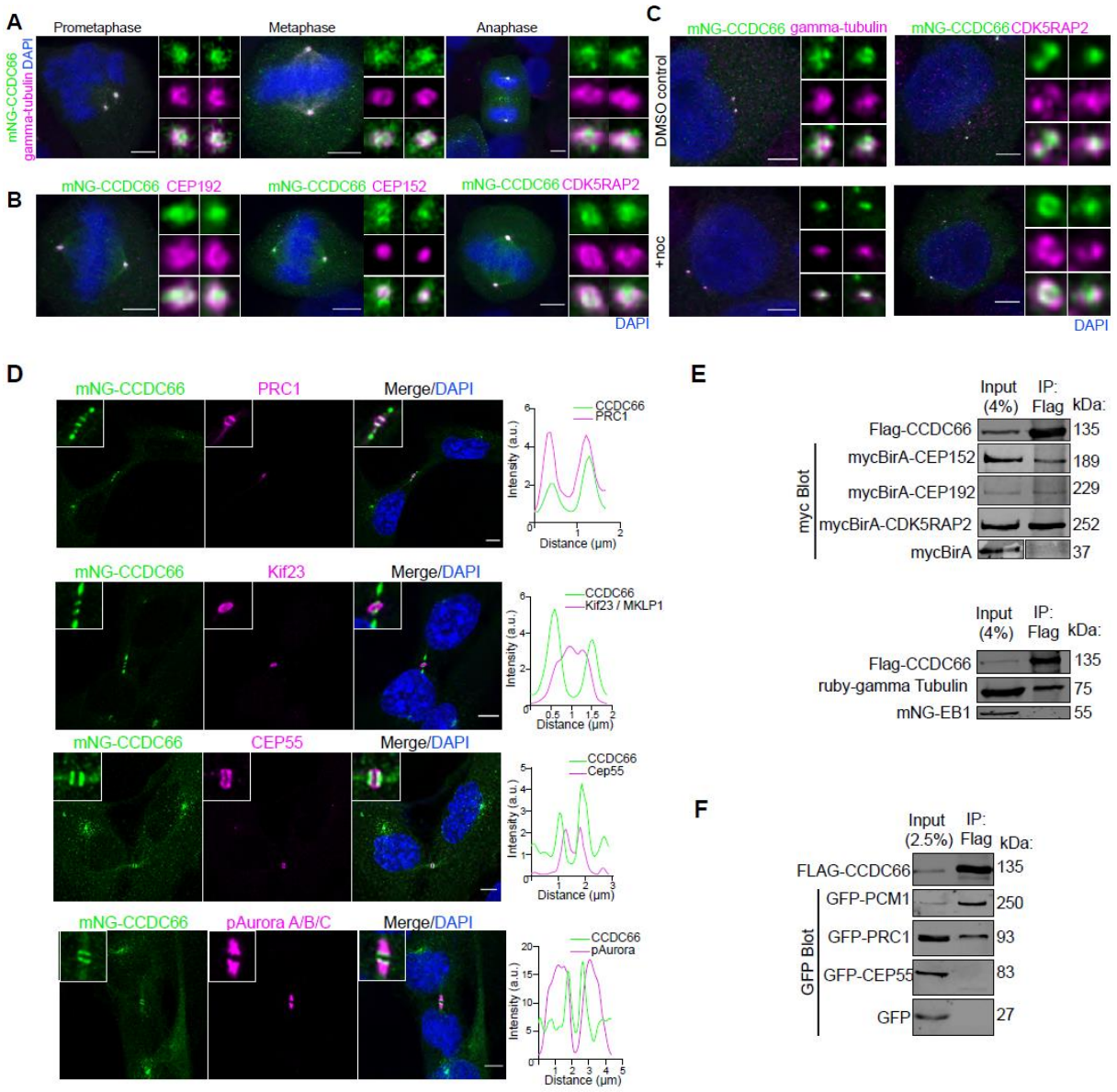

Figure 6. CCDC66 co-localizes and interacts with PCM proteins and spindle/midbody MAPs

(A)mNG-CCDC66 localizes to the centrosome throughout the cell cycle. U2OS::mNGCCDC66 cells were fixed with 4% PFA and stained for gamma-tubulin and DAPI. Still deconvolved confocal images represent centrosomal co-localization of mNG-CCDC66 with gamma-tubulin during different stages of cell division. Scale bar: 5 µm, insets show 4X magnifications of the centrosomes.

(B) Localization of mNG-CCDC66 in U2OS cells relative to Pericentriolar Material (PCM) proteins. U2OS::mNG-CCDC66 cells were fixed with 4% PFA and stained for CEP192, CEP152, or CDK5RAP2 and DAPI. Deconvolved confocal images represent their relative

localization at the spindle poles during metaphase. Scale bar: 5 µm, insets show 4X magnifications of the centrosomes.

(C) Effect of microtubule depolymerization on CCDC66 localization at the centrosome. U2OS::mNG-CCDC66 cells were treated with 0.1% DMSO or 5 µg/ml nocodazole for 1h. Cells were then fixed with 4% PFA and stained for gamma-tubulin or CDK5RAP2 and DAPI. Scale bar: 5 µm, insets show 4X magnifications of the centrosomes.

(D) Localization of mNG-CCDC66 in RPE1 cells relative to midbody proteins. RPE1::mNG-CCDC66 cells were fixed with methanol and stained for mNeonGreen and PRC1, Cep55, Kif23 (MKLP1) or pAurora A/B/C and DAPI. Graphs show the plot profiles to assess co-localization with the indicated marker. Using ImageJ, a straight line was drawn on the midbody and intensity along the distance was plotted on Graphpad Prism.

(E) Co-immunoprecipitation of Flag-CCDC66 with PCM proteins from HEK293T cells. Flag-CCDC66 was co-transfected with myc-BirA-Cep192, myc-BirA-Cep152, myc-BirACDK5RAP2, myc-BirA-PLK1 or myc-BirA in HEK293T cells. Flag-CCDC66 was precipitated with Flag beads and input and eluates (IP) were blotted with Flag and myc antibodies to assess the interaction. HEK293T cells were also co-transfected with Flag-CCDC66 and Ruby-Gamma-tubulin-T2A-mNG-EB1 fusion construct. Flag-CCDC66 was precipitated with Flag beads and Input and eluates (IP) were blotted with Flag, EB1 and gamma tubulin antibodies.

(F) Co-immunoprecipitation of Flag-CCDC66 with midbody proteins from HEK293T cells. Flag-CCDC66 was co-transfected with GFP, GFP-Cep55 or GFP-PRC1 in HEK293T cells. Flag-CCDC66 was precipitated with Flag beads and Input and eluates (IP) were blotted with Flag and GFP antibodies to assess the interaction.

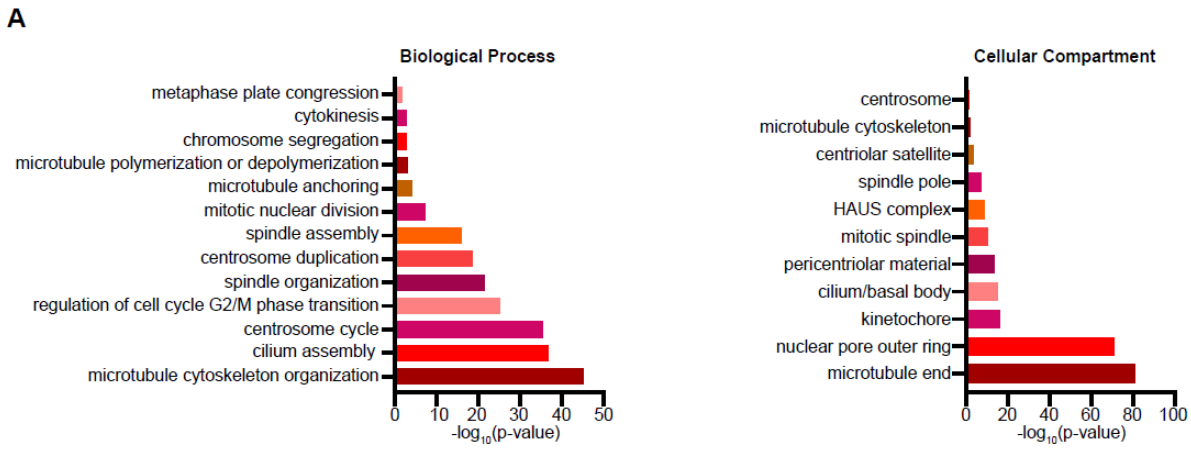

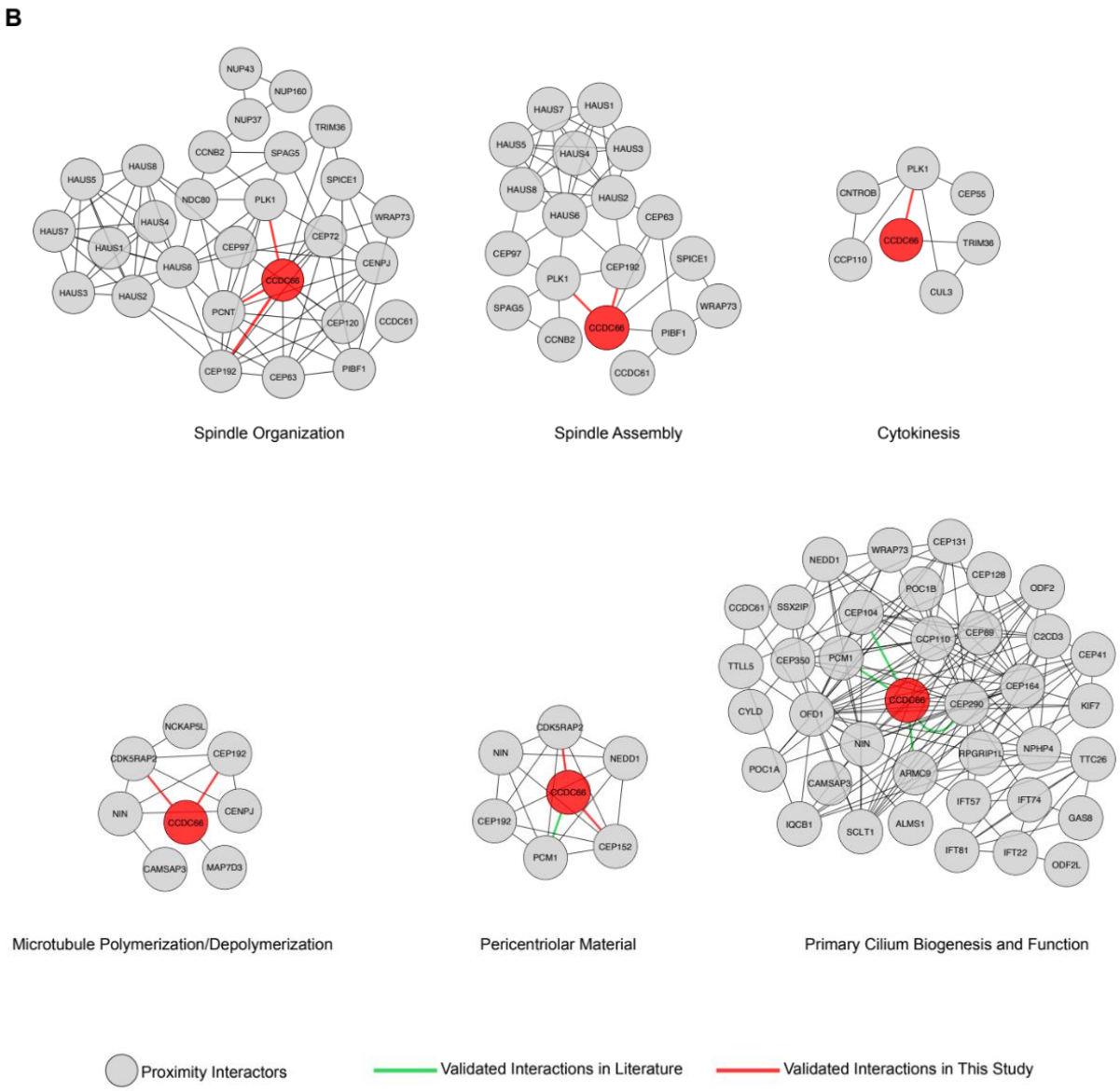

Figure 7. Gene Ontology analysis of the CCDC66 proximity interactome

(A, B) GO-enrichment analysis of the CCDC66 proximity interactors based on their (A) biological process and (B)cellular compartment. The x-axis represents the log transformed p-value (Fisher's Exact Test) of GO terms. (B) Sub-interaction networks of CCDC66 based on biological process and cellular compartment. The CCDC66 proximity interactors were grouped into clusters using gProfiler functional annotation tool. The interaction networks for the biological processes spindle organization, spindle assembly, cytokinesis, and microtubule polymerization or depolymerization were visualized using Cytoscape. The interaction networks for the cellular compartments the pericentriolar material and cell projection were also visualized. The interconnectedness among the proteins of each network was determined by the

STRING database. Edges in green color indicate the published physical CCDC66 interactors, and edges in red color indicate the proximate interactors validated in this study.

2.3 CCDC66 is required for mitotic progression

To elucidate CCDC66 functions during mitotic and cytokinetic progression, we performed loss-of-function experiments by RNAi-mediated depletion of CCDC66 using an siRNA validated in depletion and rescue experiments (Conkar et al., 2017). Given that CCDC66 localization and dynamics in dividing cells were similar in both RPE1 and U2OS cells (Fig. 4, 5), we chose U2OS cells for further characterization as a p53- responsive transformed cell (McKinley and Cheeseman, 2017). Immunoblotting of lysates prepared from U2OS cells 48 h after transfection with control and CCDC66 siRNA confirmed efficient depletion of CCDC66 in U2OS cells (Fig. 9A). To investigate the role of CCDC66 in the dynamic events of the cell cycle, we performed time lapse confocal imaging of control and CCDC66-depleted U2OS cells that stably express the chromosome marker mCherry-H2B (Fig. 8A). First, we compared the mitotic time as the time from nuclear envelope breakdown to anaphase for the control and CCDC66- depleted cells that completed mitosis and found that it increased about 1.4-fold in CCDC66-depleted cells relative to control cells (siCCDC66: 39.2 ± 8.6 min, siControl: 27.1 ± 6.6 min) (Fig. 8B). The remaining mitotic cells that did not complete mitosis during 16 h of live imaging had two different fates. They either exhibited prometaphase arrest, with some cells reaching chromosome alignment followed by metaphase plate regression or underwent apoptosis (Fig. 8A, 8C, 8D). We assessed apoptosis by membrane blebbing and DNA fragmentation and found that 23.3 ± 3.7% percent of CCDC66-depleted cells died after prolonged mitosis as compared to 8.8 ± 3.6% of control cells (Fig. 8C). Of note, scoring the percentage of cells positive for the mitotic marker phospho-H3, we found that the mitotic index was not altered upon CCDC66 loss, which might be due to increased apoptosis counteracting the delayed mitosis (Fig. 9B, 9C), which might be due to increased apoptosis in U2OS cells as a response to the delayed mitosis followed by mitotic failure. Time lapse imaging of dividing CCDC66-depleted cells also revealed formation of binucleated cells and possible cytokinesis failure (Fig. 8A).

To further define its functions during mitotic progression, we examined whether CCDC66 depletion leads to the accumulation of cells at a particular stage of mitosis by scoring cells based on their chromosome positioning and spindle organization using DNA and MT staining (Baudoin and Cimini, 2018) (Fig. 8E). CCDC66 depletion led to a higher fraction of cells in prometaphase, suggesting the presence of chromosome and spindle-related defects (Fig.

8E, 8F). In agreement, we noted that the MT arrays of the bipolar spindle, central spindle and midbody of CCDC66-depleted cells were disorganized and prominent defects in the assembly and organization of the bipolar spindle, central spindle and midbody such as disorganized MTs and reduced MT intensities (Fig. 8E). In addition to spindle phenotypes, we also examined CCDC66 function in chromosome alignment and segregation. To quantify chromosome alignment, we measured the ratio of the width to the height of the chromosomal mass, which was previously described as the chromosome congression index (Green and Kaplan, 2003; Huhn et al., 2017) (Figure 8G). CCDC66-depleted cells had a higher chromosome congression index than control cells, which indicates defective chromosome alignment at the metaphase plate. Moreover, the percentage of cells with lagging chromosomes, but not with misaligned chromosomes, increased in CCDC66-depleted cells relative to control cells (Fig. 8H). Taken together, our findings show that CCDC66 is required for mitotic progression and suggest that it might regulate spindle assembly and organization during mitosis.

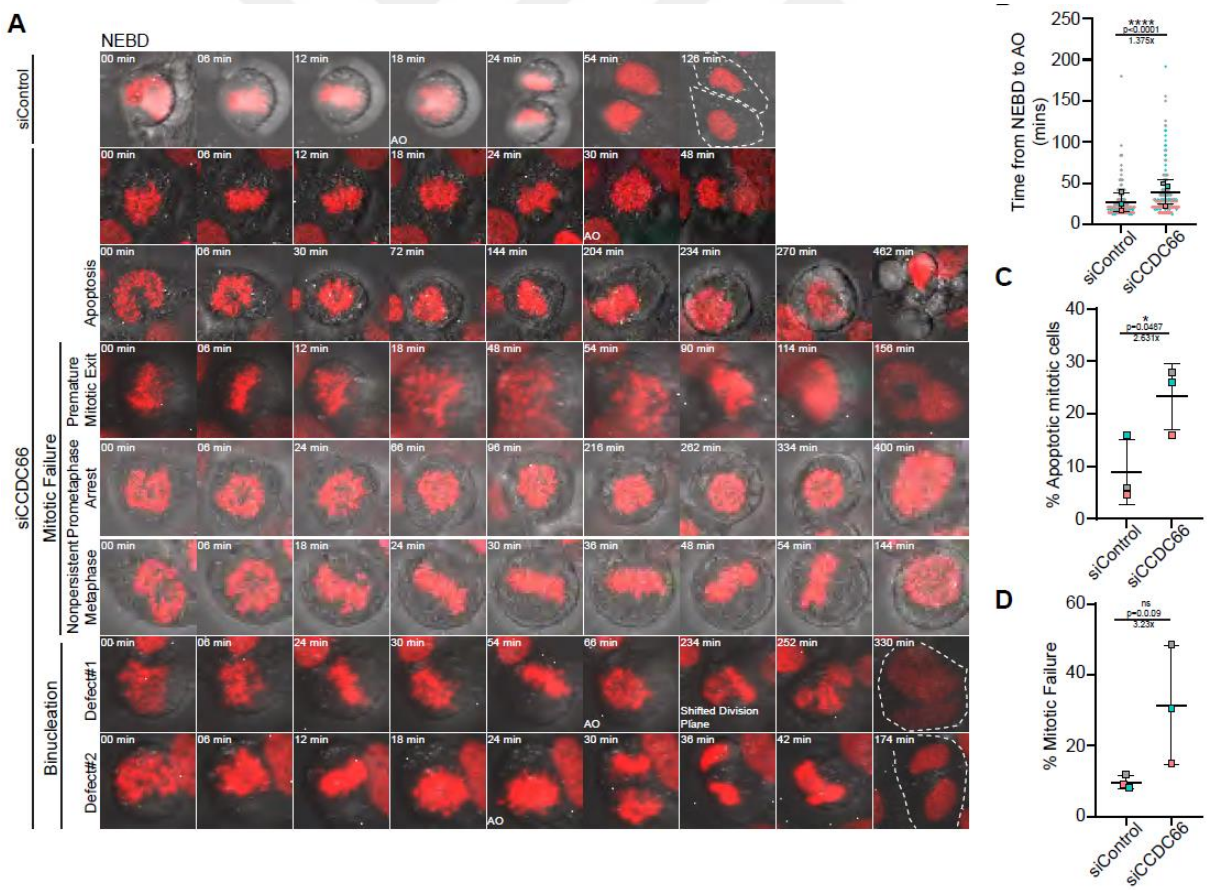

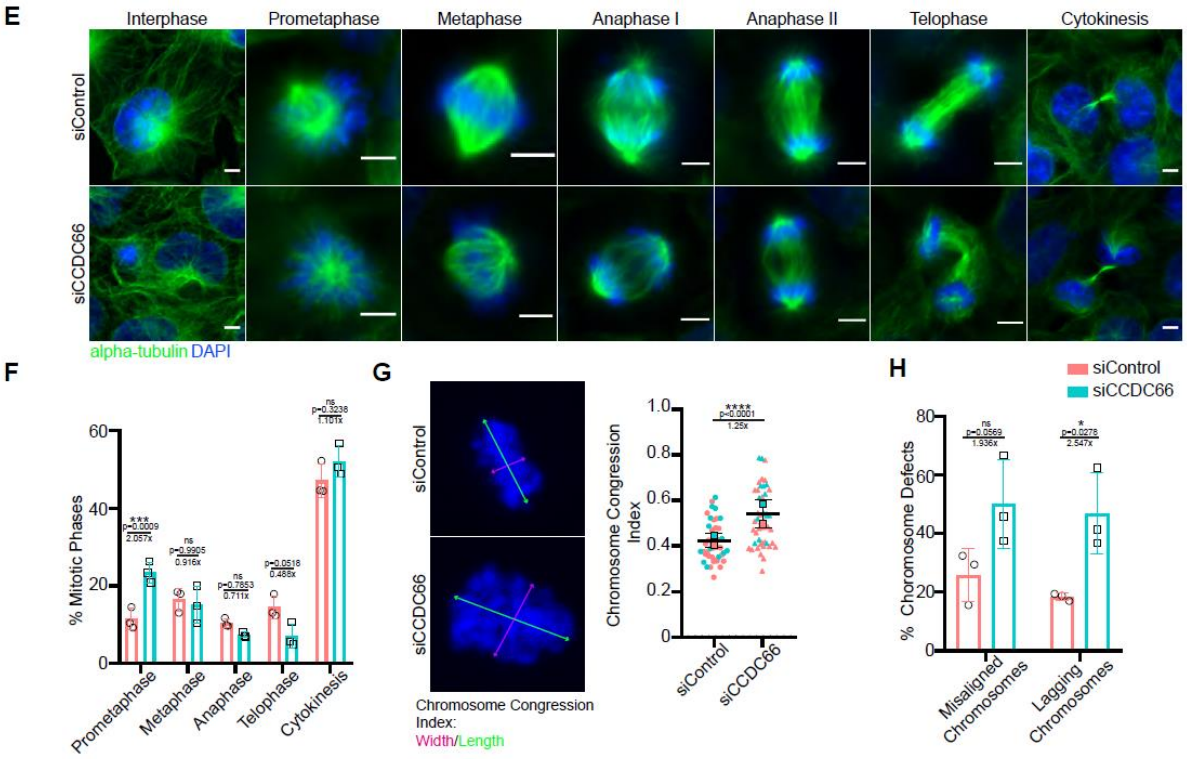

Figure 8. CCDC66 is important for faithful mitotic progression and cytokinesis

(A) Effects of CCDC66 depletion on mitotic progression. U2OS::mcherry-H2B cells were grown on 2-well Lab-Tek plates and transfected with non-targeting (siControl) or CCDC66 targeting (siCCDC66) siRNA. After 48h of transfection, cells were imaged with confocal microscopy with 20x objective. Images are acquired every 6 mins for 16h. (A) Representative still images from live imaging. Phenotypic categories for siCCDC66 include apoptosis, premature mitotic exit, prometaphase arrest and non-persistent metaphase.

(B) Quantification of mitotic time from A. Mitotic time was quantified as the time interval from nuclear envelope breakdown (NEBD) to anaphase onset (AO). Data represents the mean ±SEM of three independent experiments and is plotted using super-plot.

(C) Quantification of percent mitotic cell death from A. Mitotic cell death represents mitotic cells that underwent apoptosis during the time of imaging. Data represents the mean ±SEM of three independent experiments and is plotted using super-plot.

(D) Quantification of percent mitotic failure from A. Mitotic failure refers to the cells that entered mitosis but could not proceed through anaphase because of; premature mitotic exit, prometaphase arrest and non-persistent metaphase. Data represents the mean ±SEM of three independent experiments and is plotted using super-plot.

(E) Spindle and chromosome phenotypes of CCDC66-depleted cells. Representative images of different stages of cell division for siControl and siCCDC66 transfected U2OS cells are shown. Cells were transfected with either siControl or siCCDC66, fixed with methanol 48h post-transfection and stained for α-tubulin and DAPI. Mitotic cell stages were categorized based on DNA staining. Scale bar: 5 μm

(F) Quantification of E. Data represents mean ±SEM of three independent experiments. n>1000 for all experiments. Mean prometaphase percentage is 11.42 for siControl and mean prometaphase percentage is 23.50 for siCCDC66. (***$p<0.001$, ns not significant)

(G) CCDC66 depletion increases chromosome width. U2OS cells were transfected with siRNA, fixed with methanol, and stained for DAPI. Chromosome congression index is measured by dividing the length of the metaphase plate by its width. Data represent the mean ±SEM of two independent experiments. (****$p<0.0001$). Scale bar: 5 μm.

(H) Quantification of chromosome alignment and segregation defects from A. The quantification shows the number of metaphase cells that have misaligned chromosomes and anaphase and telophase cells that have lagging chromosomes. Data represent the mean ±SEM of three independent experiments. (ns not significant).

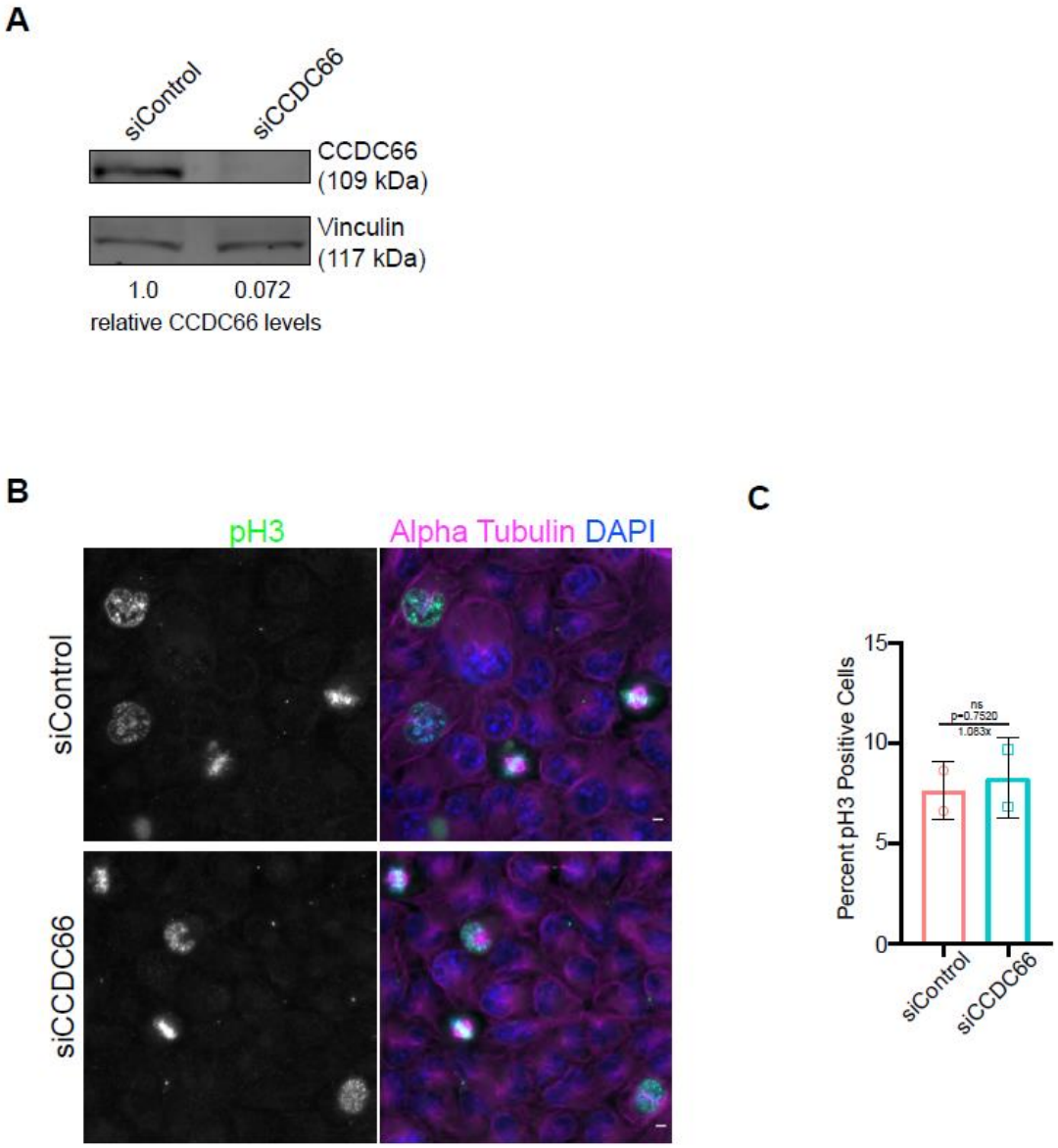

Figure 9. CCDC66 depletion does not alter total mitotic index

(A) Validation of the efficiency of RNAi-mediated CCDC66 depletion. U2OS cells were transfected with siControl or siCCDC66. 48 h after post-transfection, cell extracts immunoblotted for CCDC66 and vinculin (loading control). Band intensities were measured on ImageJ and normalized against background and vinculin intensities. Arbitrary value is determined based on siControl.

(B) Effect of CCDC66 depletion on mitotic index. U2OS cells were transfected with control or CCDC66 siRNA, fixed with methanol 48 h post-transfection and stained for the mitotic marker phospho-Histone3 (pH3), α-tubulin and DAPI. Representative images are shown. Scale bar: 5 μm.

(C) Quantification of B. Mitotic cells are counted based on DNA staining. Data represent the mean ±SEM of two independent experiments. n>1000 for all experiments. Mean mitotic cell number for siControl is 10.31 and mean mitotic cell number for siCCDC66 is 12.49.

2.4 CCDC66 is required for spindle organization and positioning

To uncover the molecular defects that underlie defective mitotic progression associated with CCDC66 depletion, we investigated the phenotypic consequences of CCDC66 depletion on spindle architecture and positioning. Relative to control cells, CCDC66 depletion resulted in shorter average spindle lengths, which was measured as pole-to pole distance in metaphase cells (Fig. 10A). However, it did not compromise spindle pole morphology and spindle pole integrity, which is quantified as the spindle pole width (Fig. 10A). We also measured the angle between the spindle axis and the substratum, which revealed an increase from 7.7 ± 0.3º in control cells to 13.1 ± 1.5º in CCDC66-depleted cells (Fig. 10A). Because astral MTs are essential for spindle orientation (Lu and Johnston, 2013), the spindle positioning phenotype might be due to defects in astral MT assembly and stability. To investigate this, we quantified the astral MT fluorescence intensity and length in control and CCDC66-depleted cells and found that they were both reduced upon CCDC66 loss (Fig. 10B, 10C). Given the role of CCDC66 during astral MT assembly and/or stability, we next examined how CCDC66 loss affects tubulin levels at the metaphase spindle. The tubulin fluorescence intensity at the spindle decreased

about 0.6-fold in CCDC66-depleted cells relative to control cells (Fig. 10B, 10C). Immunoblotting of lysates prepared from control and CCDC66 siRNA-transfected cells showed that the intensity changes in spindle MTs were not due to altered cellular abundance of alpha-tubulin (Fig. 11A).

Spindle density and length defects could be caused by compromised interpolar MTs and K-fiber integrity (Dumont and Mitchison, 2009). Moreover, impaired K-fiber formation and stability could underlie chromosome congression defects. Therefore, we tested whether and if so how CCDC66 regulates K-fibers by performing cold stability assay, in which K-fibers are visualized by selective depolymerization of less stable interpolar and astral MTs by cold treatment of cells for 10 minutes at 4°C (Brinkley and Cartwright, 1975; Rieder, 1981). The tubulin fluorescence intensity of K-fibers was reduced in CCDC66-depleted cells relative to control cells (Fig. 10D). This result identifies CCDC66 as a regulator of K-fiber integrity, which explains the chromosome alignment defects and mitotic failure observed in CCDC66-depleted

cells (Fig. 8). Notably, mNG_CCDC66 still localized to the spindle microtubules in cold-treated cells, identifying it as a K-fiber protein. Together, our findings indicate that CCDC66 regulates spindle assembly and positioning to ensure proper mitotic progression.

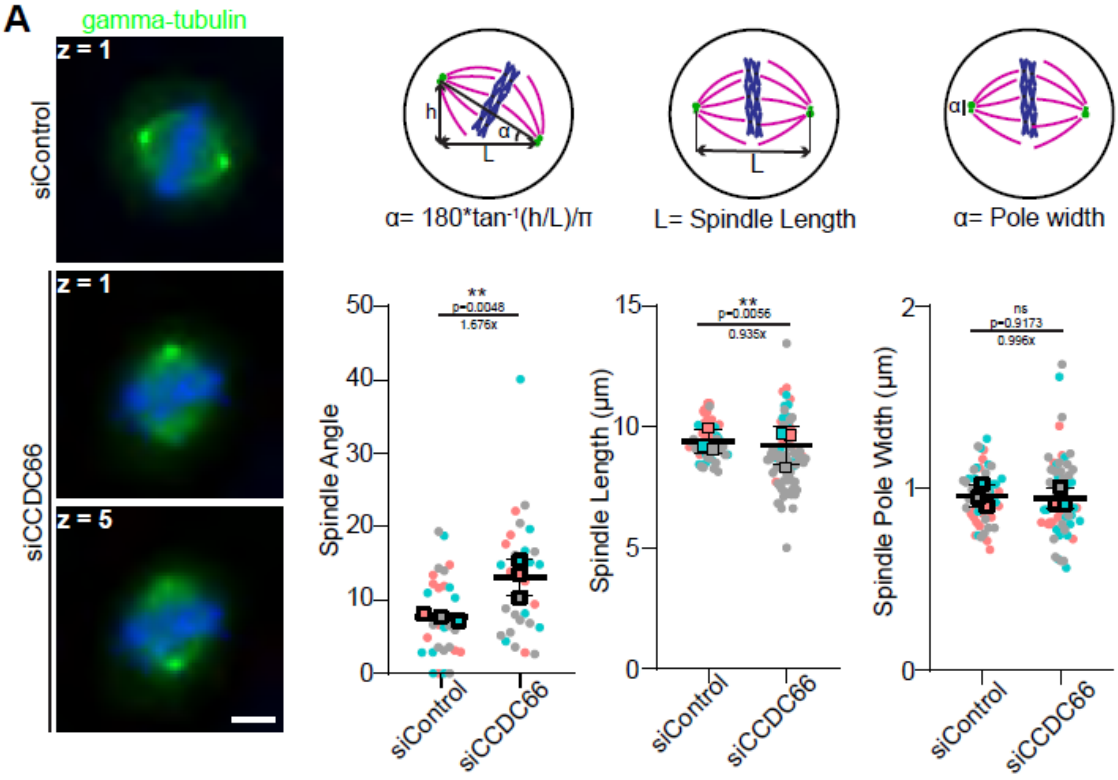

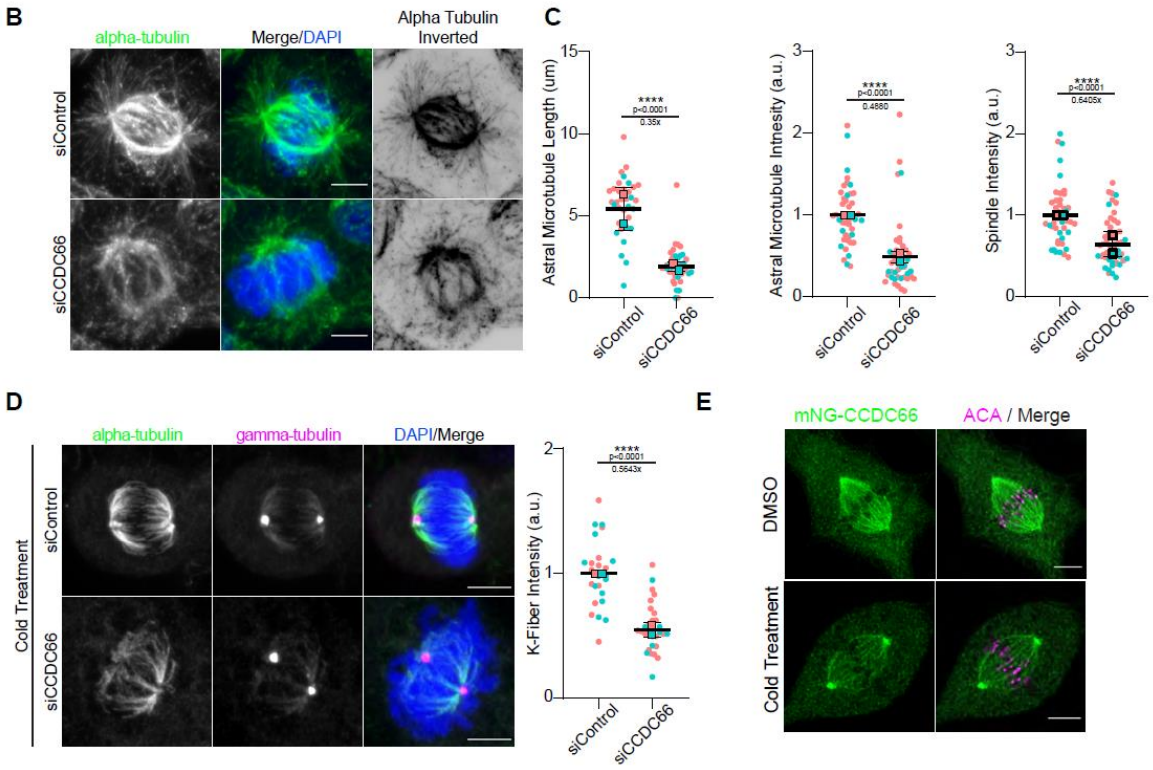

Figure 10. CCDC66 regulates spindle organization and positioning

(A) Effects of CCDC66 depletion on spindle angle, length and pole width. U2OS cells were transfected with control and CCDC66 siRNA, fixed with methanol and stained for γ-tubulin. z on still images indicates the stack where the spindle pole is found. Spindle angle is calculated by the formula α=180*tan-1(h/L)/π where h represents the stack difference between two spindle poles, L represents the distance between spindle poles. Spindle length is calculated by measuring the distance between two spindle poles. Spindle pole width is calculated by measuring the length of the pericentriolar material of the spindle pole. Data represent the mean ±SEM of three independent experiments. (**p<0.01, ns not significant). Scale bar: 5 μm.

(B) Spindle microtubule density and astral microtubule length is reduced in CCDC66 depleted cells. U2OS cells were transfected with siRNA then fixed with methanol and stained for α-tubulin and DAPI. Representative images are shown. Inverted image is shown to emphasize astral microtubules better. Scale bar: 5 μm.

(C) Quantification of (B). Astral microtubule and spindle microtubule intensity were measured on ImageJ by taking several points on the spindle to measure the intensity and subtracting the background mean intensity. Data represent the mean ±SEM of three independent experiments. (****p<0.0001).

(D) CCDC66 depletion reduces K-fiber intensity. Cells were transfected with siRNA then after 48 h after transfection, cells were incubated in ice for 10 mins. Cells were fixed with methanol and stained for alpha tubulin, gamma tubulin, and DAPI. K-fiber intensity was measured as described for (C). (****p<0.0001). Scale bar: 5 μm.

(E) CCDC66 localizes to K-fibers. RPE1::mNG-CCDC66 stable cell line was incubated in ice for 10 mins and fixed with MeOH then stained for mNG and anticentromeric antibody (ACA). Images represent a single stack and were captured with the same camera settings from the same coverslip. Scale bar: 5 μm.

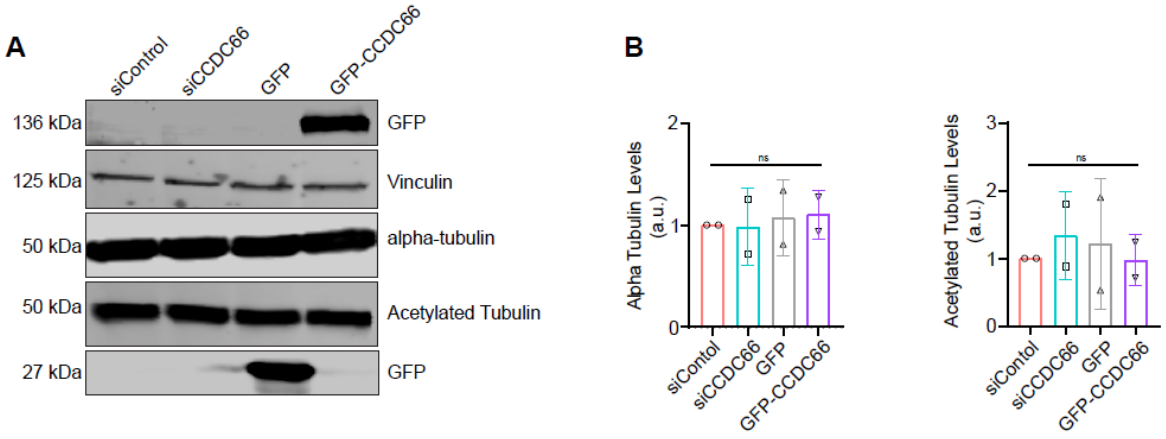

Figure 11. Effects of CCDC66 depletion and overexpression on cellular abundance of tubulin and acetylated tubulin

(A) Cellular abundance of tubulin and acetylated tubulin in control, CCDC66-depleted and GFP-CCDC66-overexpressing cells. Cells are transfected with siRNA or GFP control and GFP-CCDC66 constructs. After 48 h the lysates are collected and immunoblotted for GFP, α-tubulin, acetylated tubulin, and vinculin (loading control).

(B) Quantification of A. Data represents mean ±SEM of two independent experiments. (ns not significant).

2.5 CCDC66 is required for centrosome maturation and MT nucleation during mitosis

Given that CCDC66 interacts with PCM proteins implicated in centrosome maturation and its loss results in mitotic and spindle defects, we hypothesized that CCDC66 might function in these processes by regulating MT nucleation during mitosis. To test this, we synchronized control and CCDC66-depleted cells using the Eg5-inhibitor S-trityl-Lcysteine (STLC) and performed MT regrowth experiments in mitotic cells (Fig. 12A). MT depolymerization was induced by nocodazole treatment, and cells were then fixed and stained for MTs and gamma-tubulin at the indicated time points after nocodazole washout (Fig. 12A). The MT aster size was

reduced in CCDC66-depleted cells relative to control cells at 5, 8 and 10 min after washout, which indicates MT nucleation defects (Fig. 12A, 12B). Notably, CCDC66-depleted cells had an increased number of MT nucleating centers than control cells, suggesting possible activation of non-centrosomal MT nucleation pathways (Fig. 13A). CCDC66-depleted cells were also delayed in the formation of the bipolar spindle after nocodazole treatment (Fig. 12C, 12D). By 40 min, 30.9 ± 2.6% control cells and 9.9 ± 0.2% CCDC66-depleted cells formed a bipolar spindle (Fig. 12C, 12D). Supporting its roles in centrosome-mediated MT nucleation, gamma-tubulin levels at the spindle poles were reduced to 0.7-fold in CCDC66-depleted cells relative to control cells (Fig. 12E). In a complementary approach, ultrastructure expansion microscopy (U-ExM) analysis of STLC-synchronized G2 and mitotic cells confirmed reduced gamma-tubulin recruitment to the PCM and spindle MTs upon CCDC66 depletion (Fig. 13C). We also noted that organization of gamma-tubulin at the PCM was disrupted while its centriolar lumenal pool remained intact (Fig. 13C).

During centrosome maturation, centrosomes recruit more PCM proteins to increase their MT-nucleating capacity. In particular, CDK5RAP2, CEP192, CEP152 and Pericentrin are required for spindle pole recruitment of gamma-tubulin (Luders, 2012; Palazzo et al., 2000). Given that CCDC66 interacts with these proteins, we tested their centrosomal targeting as a potential mechanism by which CCDC66 regulates centrosome maturation. To test this, we quantified centrosomal levels of these PCM proteins in control and CCDC66 siRNA-transfected cells. The levels of CDK5RAP2 and Pericentrin, but not CEP192 and CEP152, were significantly reduced at the spindle poles in CCDC66-depleted cells as compared to control cells (Fig. 12F, 12G, 13D, 13E). Immunoblot analysis of lysates form control and CCDC66-depleted cells with antibodies against these proteins indicated that CCDC66 loss does not alter their cellular abundance (Fig. 13B). Collectively, these results demonstrate that CCDC66 functions during mitotic MT nucleation in part by centrosomal targeting of CDK5RAP2 and Pericentrin and thereby gamma-tubulin.

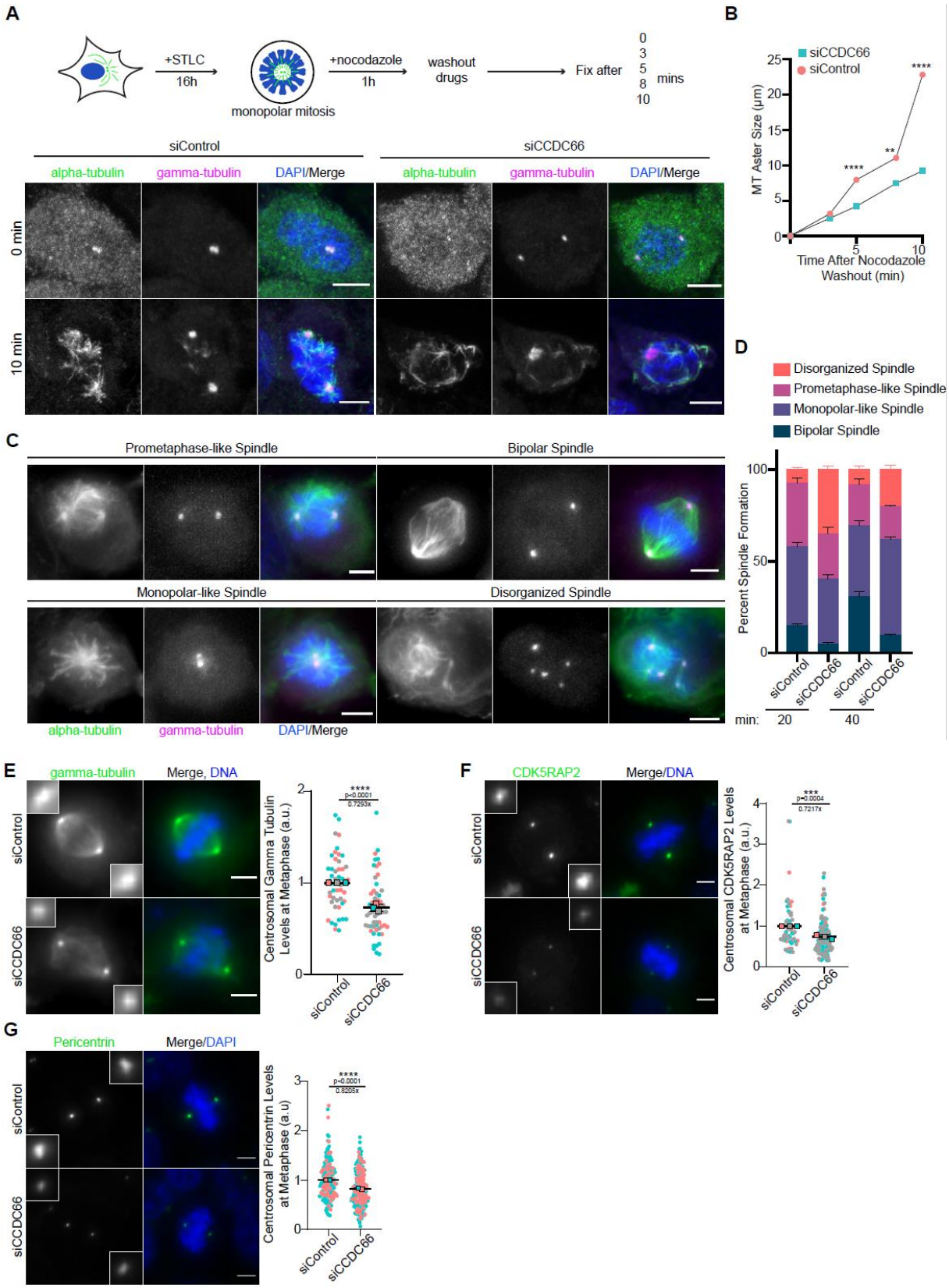

Figure 12. CCDC66 recruits core PCM proteins to the centrosome and is required for mitotic microtubule nucleation

(A) CCDC66 depletion slows down microtubule nucleation in mitotic cells. As illustrated in the experimental plan, U2OS cells were transfected with control and CCDC66 siRNA. 48 h post-transfection, they were synchronized with 5 μM STLC treatment for 16h. After cell synchronization, microtubules were depolymerized by nocodazole treatment for 1h. Following nocodazole wash out, cells were fixed and stained for alpha-tubulin, gamma tubulin and DAPI at the indicated time points.

(B) Quantification of A. For quantification of microtubule aster size, microtubule nucleation area is measured on ImageJ using polygon selection tool. Data represent the mean ±SEM of two independent experiments. (****$p<0.0001$, **$p<0.01$). Scale bar: 5 μm.

(C) Effect of CCDC66 depletion on bipolar spindle assembly. Control and CCDC66 siRNA-transfected cells were stained with alpha-tubulin, gamma-tubulin and DAPI.

(D) Quantification of C. Mitotic cells were scored based on their spindle architecture as bipolar spindle, monopolar spindle, prometaphase-like spindle, and disorganized spindle. Data represent the mean ±SEM of two independent experiments. Scale bar: 5 μm.

(E-G) Effects of CCDC66 depletion on abundance of PCM proteins at the spindle poles. U2OS cells were transfected with control and CCDC66 siRNA. After 48 h, cells were fixed with methanol and stained for (C) gamma-tubulin, (D) CDK5RAP2, (E) Pericentrin, and DAPI. Centrosomal abundance of PCM proteins was measured on ImageJ by drawing a 3.4 μm2 circular area. Data represent mean ±SEM of two (Pericentrin) and three (gamma-tubulin, CDK5RAP2) independent experiments. (****$p<0.0001$). Images for each panel represent cells captured with the same camera settings from the same coverslip. Scale bar: 5 μm.

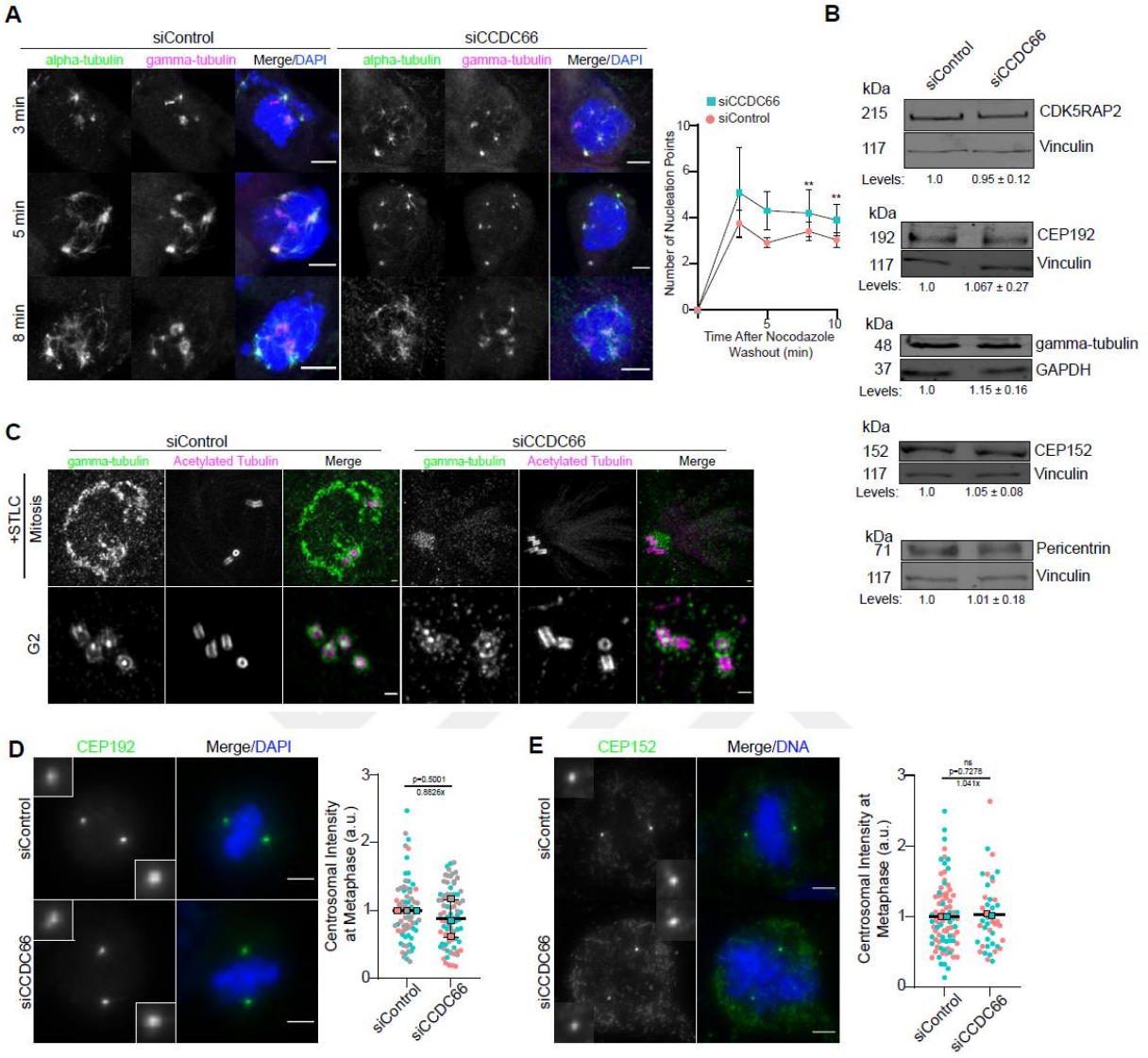

Figure 13. CCDC66 depletion interferes with centrosome maturation and microtubule nucleation.

(A) Quantification of microtubule nucleation sites following nocodazole washout of STLC-synchronized control and CCDC66-depleted cells. Representative images are shown for control and CCDC66-depleted cells. The graph indicates the number of microtubule nucleation points that are counted from gamma-tubulin and alpha-tubulin signals. Data represent the mean ±SEM of two independent experiments. (**p<0.01) Scale bar: 5 μm.

(B) Effect of CCDC66 depletion on the cellular abundance of PCM proteins. U2OS cells were transfected with siControl or siCCDC66, and 48 h after transfection extracts from cells were immunoblotted for Cdk5Rap2, Cep192, Cep152, γ-tubulin or Pericentrin and vinculin (loading control) or GAPDH (loading control). Band intensities were measured on ImageJ and

normalized against background and vinculin intensities. Data represent the mean ±SEM of three independent experiments.

(C) Ultrastructure expansion microscopy (U-ExM) analysis of control and CCDC66 depleted cells. U2OS cells were transfected with control and CCDC66 siRNA. 48 post transfection, cells were synchronized by 16 h STLC treatment and prepared for imaging. Cells were stained for gamma-tubulin and acetylated tubulin, imaged using confocal microscopy and deconvolved. Mitotic and G2 cells were picked for representation.

2.6 CCDC66 controls cytokinetic progression and geometry of cleavage furrow ingression

In addition to mitotic defects, we observed that CCDC66 depletion interfered with progression of cytokinesis and caused an increase in the percentage of binucleated cells in a time course manner (Fig. 14A, 14B). Time lapse imaging of dividing CCDC66-depleted cells revealed two different events that resulted in binucleated cells (Fig. 8A). First phenotype was the regression of the cleavage furrow after chromosome segregation. Second phenotype was failure in forming the cleavage furrow and initiating cytokinesis (Fig. 8A). During the analysis of CCDC66-depleted cells stained for MTs, we noted that the cleavage furrow ingression is highly asymmetric and/or skewed in a significant number of cells (Fig. 14C). In fact, about 63.8% of CCDC66-depleted cells had this architectural defect relative to 23.8% in control cells (Fig. 14D). These results support the functions of CCDC66 during organization of MTs at the midbody.

Depletion of central spindle and midbody-associated proteins such as PRC1 causes defective cytokinesis, which leads to multinucleation and polyploidy (Gruneberg et al., 2006; Jiang et al., 1998; Mollinari et al., 2002; Zhu and Jiang, 2005). Given that CCDC66 interacts with PRC1, we tested whether cytokinetic defects of CCDC66 are caused by defects in PRC1 targeting to the central spindle and midbody. The fluorescence intensities of PRC1 at the central spindle and midbody were comparable between control and CCDC66-depleted cells, indicating that CCDC66 is not required for PRC1 recruitment to the central spindle (Fig. 14E, 14F). Asymmetric furrow ingression and skewed central spindles and midbody upon CCDC66 loss could be due to defective recruitment of central spindle components other than PRC1.

Defects in central spindle and intercellular bridge/midbody, as well as K-fibers, which are all highly organized and stable MT bundles, could be attributed to MT bundling activity of CCDC66. To test this hypothesis, we used in vitro experiments to investigate the possible MT

crosslinking activity of CCDC66. We expressed MBP-mNG-CCDC66 in insect cells and purified it using nickel beads (Fig. 15A). As a control, we purified MBPmNG in bacteria (Fig. 15B). Using in vitro MT sedimentation assay, we showed that MBP-mNG-CCDC66 directly binds to MTs (Fig. 15A). After validation of MT affinity, we performed in vitro MT bundling assays. Incubation of MBP-mNG-CCDC66, but not MBPmNG, with taxol-stabilized rhodamine-labeled MTs resulted in the formation of MT bundles in vitro (Fig. 14G). Notably, these bundles co-localized with CCDC66, confirming its direct MT affinity. Given that the C-terminal 570-948 residues of CCDC66 binds to MTs and localizes to spindle MTs, we next asked whether this fragment bundles MTs in vitro. We expressed and purified MBP-CCDC66 (570-948) in bacteria (Fig. 15A). Like full length CCDC66, MBP-CCDC66 (570-948) associated with MTs directly and promoted MT bundling in vitro (Fig. 14H, 15A). In agreement with their in vitro activities, overexpression of mNG fusions of CCDC66 and its C-terminal (570-948) fragment induced formation of MT bundles (Fig. 15C). Notably, the bundles formed by mNGCCDC66 (570-948) were resistant to MT depolymerization (Fig. 15C). Collectively, these results demonstrate that CCDC66 is a cross-linking MAP that is required for organization of central spindle and midbody MTs during cytokinesis.

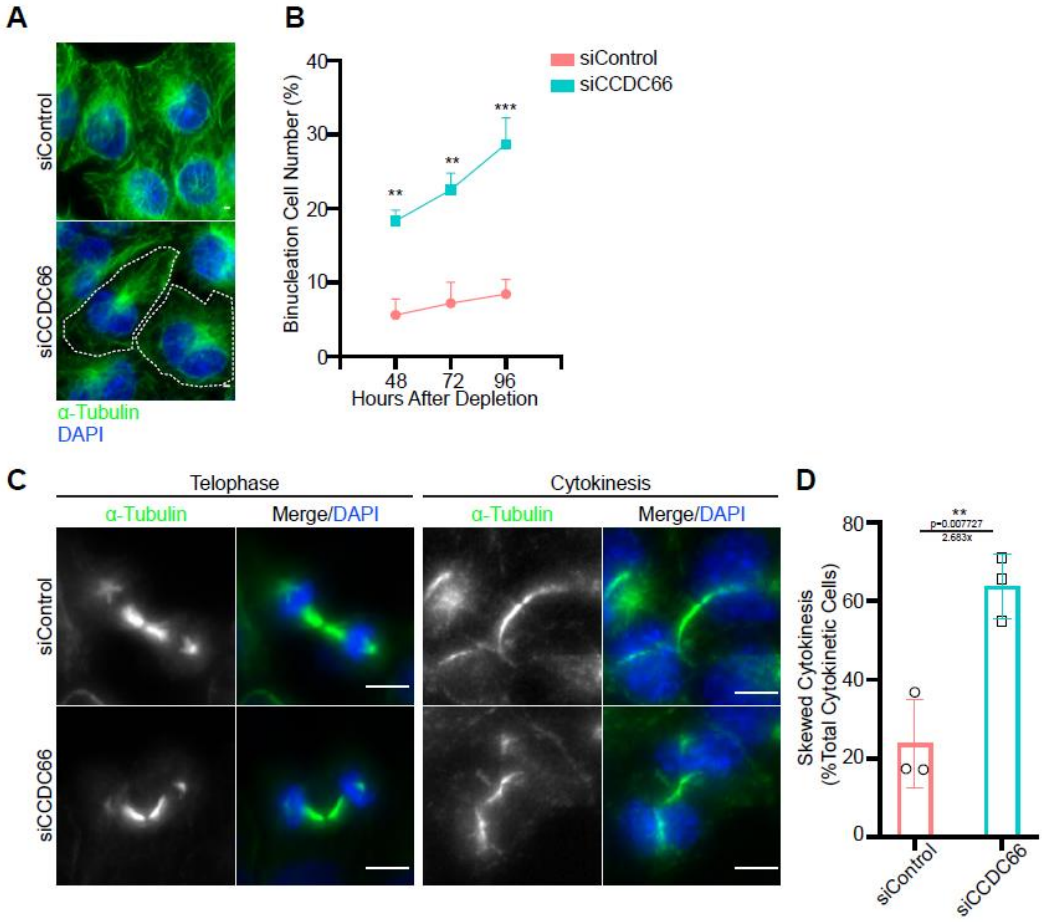

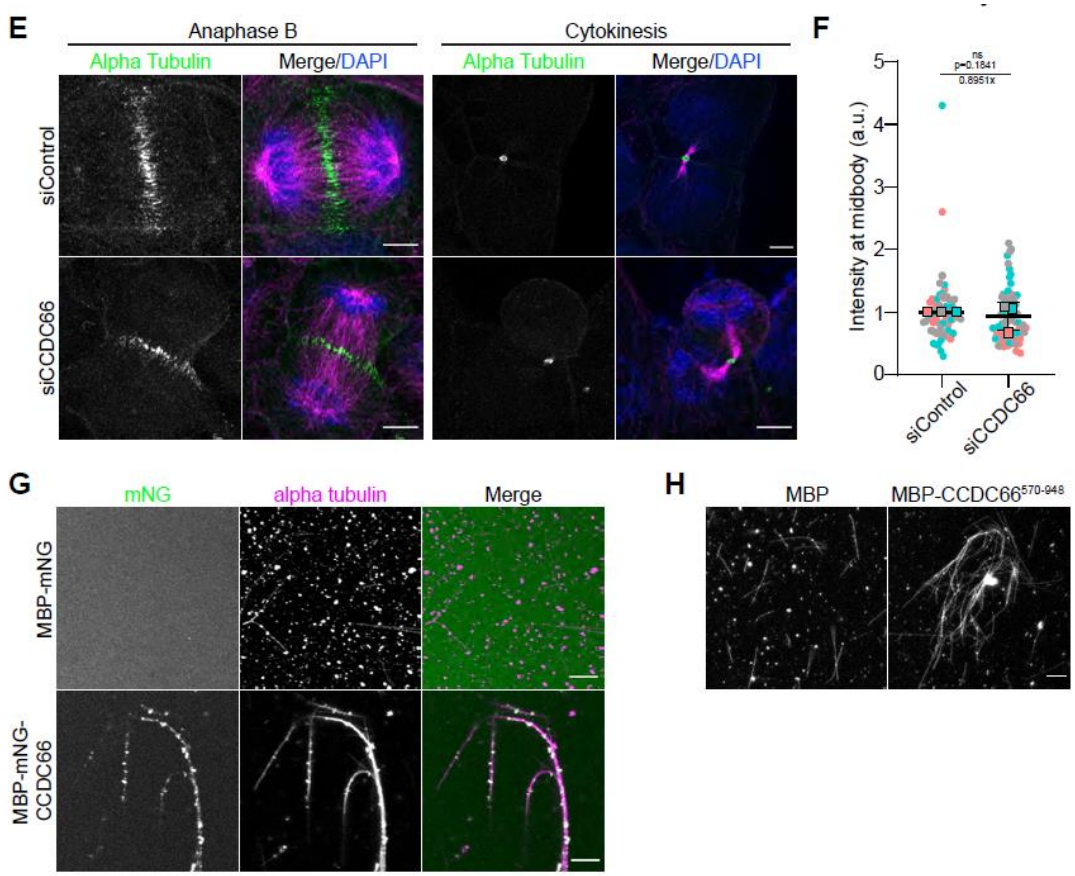

Figure 14. CCDC66 is required for cytokinesis and cleavage furrow geometry

(A) CCDC66 depletion increases binucleation. Immunofluorescence images represent siControl or siCCDC66 transfected U2OS cells. Cells were transfected with the indicated siRNAs and fixed with methanol after 48 h, 72 h, and 96 h of transfection. Binucleation is determined based on alpha-tubulin and DNA staining. Scale bar: 5 μm.

(B) Quantification of (A). Graph represents the percentage of binucleation with mean ±SEM of two independent experiments. (**p<0.01 ****p<0.0001).

(C) CCDC66 depletion leads to disorganization of central spindle structure. U2OS cells were transfected with the indicated siRNAs, fixed with methanol and stained for alpha tubulin and DAPI. Images represent telophase and cytokinetic cells. Scale bar: 5 μm.

(D) Quantification of (C). Skewed cytokinesis indicates the cells as represented in (C) for siCCDC66. Skewed cells with asymmetric cleavage furrow are counted, and percentage is calculated according to total telophase/cytokinesis cell number. Data represent the mean ±SEM of three independent experiments. (**p<0.01).

(E) CCDC66 depletion does not alter PRC1 midbody levels. U2OS cells were transfected with siRNA then fixed with methanol after 48 h and stained for PRC1, alpha tubulin and DAPI. Images represent cells from Anaphase and cytokinesis. Scale bar: 5 μm.

(F) Quantification of (E). PRC1 intensity was measured on ImageJ, the background signal was subtracted, and normalized value was multiplied with area. Arbitrary value was determined by normalizing against siControl. (ns: not significant).

(G) In vitro microtubule bundling with full length CCDC66. His-MBP-mNG-CCDC66 was purified from insect cells using Ni-NTA agarose beads and microtubule bundling was performed (see methods for detail alpha-tubulin was visualized by rhodamine labelled tubulin and CCDC66 was visualized with mNG signal. Scale bar: 5 μm.

(H) In vitro microtubule bundling with CCDC66 (570-948). His-MBG-CCDC66 (570-948) C terminal fragment was purified from bacterial culture using Ni-NTA agarose beads and microtubule bundling was performed (see methods for detail). Alpha tubulin is visualized by rhodamine labelled tubulin. Scale bar: 5 μm.

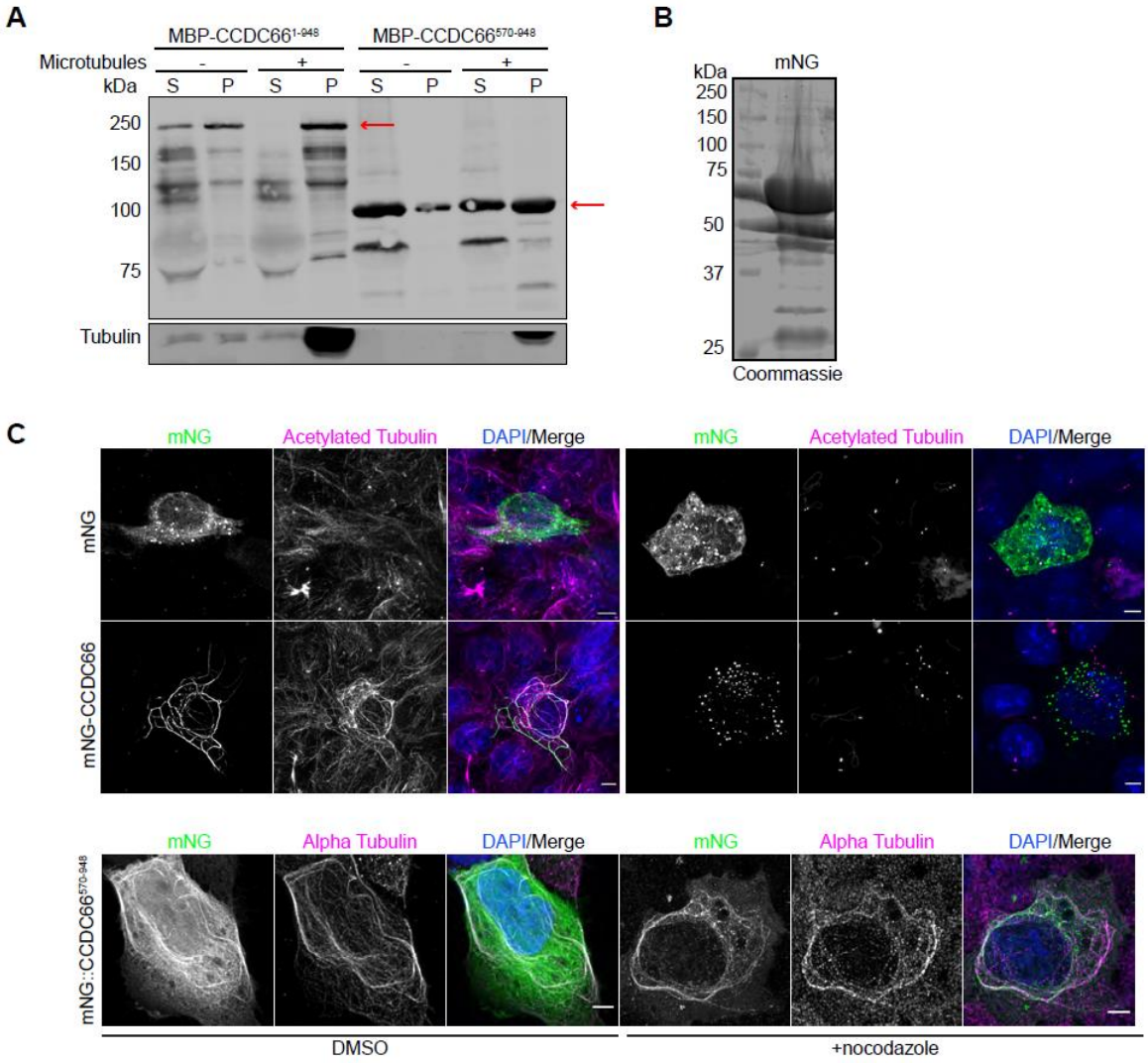

Figure 15. Validation of CCDC66 purification, microtubule association and bundling

(A) Validation of His-MBP-mNG-CCDC66 purification and direct microtubule association. His-MBP-mNG-CCDC66 was purified from insect cells using Ni-NTA agarose beads and in vitro microtubule pelleting was performed (see methods for detail). MBP-His-CCDC66 (570-948) was purified from bacterial culture using Ni-NTA agarose beads and microtubule pelleting was performed. Purified His-MBP-mNGCCDC66 full length and C-terminal fragment were run on SDS-PAGE and blotted with CCDC66 antibody. S stands for supernatant, P stands for pellet. Arrows indicate the corresponding proteins.

(B) Validation of MBP-mNG purification with Coomassie.

(C) Effect of mNG-CCDC66 and mNG-CCDC66 (570-948) overexpression on microtubule organization and stability in cells. U2OS cells were transfected with mNG, mNG-CCDC66 or mNG-CCDC66 (570-948) expression plasmids. 24 h post transfection, cells were treated with

5 μM nocodazole or 0.01% DMSO for 1 h, fixed with methanol and stained for the indicated proteins and DNA. Scale bar: 5 μm.

2.7 Expression of CCDC66 and its centrosome and MT-binding fragments restore centrosome maturation and spindle defects of CCDC66-depleted cells

The functional significance of the dynamic localization of CCDC66 to the spindle poles, centriolar satellites and MTs during cell division is not known. To address to what extent mitotic phenotypes caused by CCDC66 depletion are governed by its different cellular pools and to gain further insight into its mechanism of action, we performed phenotypic rescue experiments. To this end, we first generated three different CCDC66 siRNA resistant constructs: 1) mNG-CCDC66 to validate the specificity of the phenotypes, 2) mNG-CCDC66 (570-948) to assess the functional significance of CCDC66 localization to the spindle poles and MTs, 3) C-terminal mNG-CCDC66 fusion with the centrosomal targeting domain PACT to distinguish its centrosome-specific activities from the ones mediated by MTs and centriolar satellites. Next, we used lentiviral transduction to generate U2OS cells stably expressing these fusion proteins as well as mNG itself as a control. Finally, we stained these cells with centrosome and MT markers to validate their cellular localization. In control and CCDC66-siRNA-transfected cells, mitotic localization profiles of mNG-CCDC66 and mNG-CCDC66 (570-948) were similar to the ones we reported in Fig. 1 (Fig. 16A). We highlight that the result from CCDC66-depleted cells also confirms that the reported localizations in Fig. 1 and S1 were not due to overexpression in cells expressing endogenous protein. As for mNG-CCDC66-PACT, its localization was restricted to the centrosome and did not localize to the MTs (Fig. 16A). Of note, its centrosomal to cytoplasmic relative fluorescent intensity was much higher, indicating that the majority of cellular CCDC66 was sequestered at the centrosome (Fig. 16A).

We performed rescue experiments for defective targeting of gamma-tubulin to the spindle poles, reduced spindle tubulin intensity and shorter spindle length associated with CCDC66 loss. mNG-CCDC66 expression rescued all three phenotypes to comparable or greater levels to control siRNA-transfected mNG-expressing cells, indicating that these phenotypes are specific to CCDC66 depletion (Fig. 16A-D). mNGCCDC66 (570-948) expression also rescued all three phenotypes, suggesting that its centrosomal and MT affinity of this fragment is sufficient for CCDC66 functions in these processes (Fig. 16A-D). Notably, the average gamma-tubulin intensities at the spindle poles in these cells was greater than that of control cells, which

might be due to its higher expression generating more binding sites for gamma-tubulin. As for the spindle length and tubulin levels, not only CCDC66 (570-948) but also full length CCDC66 resulted in higher averages relative to control cells, suggesting that their expression might promote these phenotypes via increased MT nucleation. Finally, mNG-CCDC66- PACT restored all three phenotypes to comparable or higher levels than that of control cells (Fig. 16A-D). Together, these results show that centrosomal and MT pools of CCDC66 are required for its functions during centrosome maturation and spindle assembly.

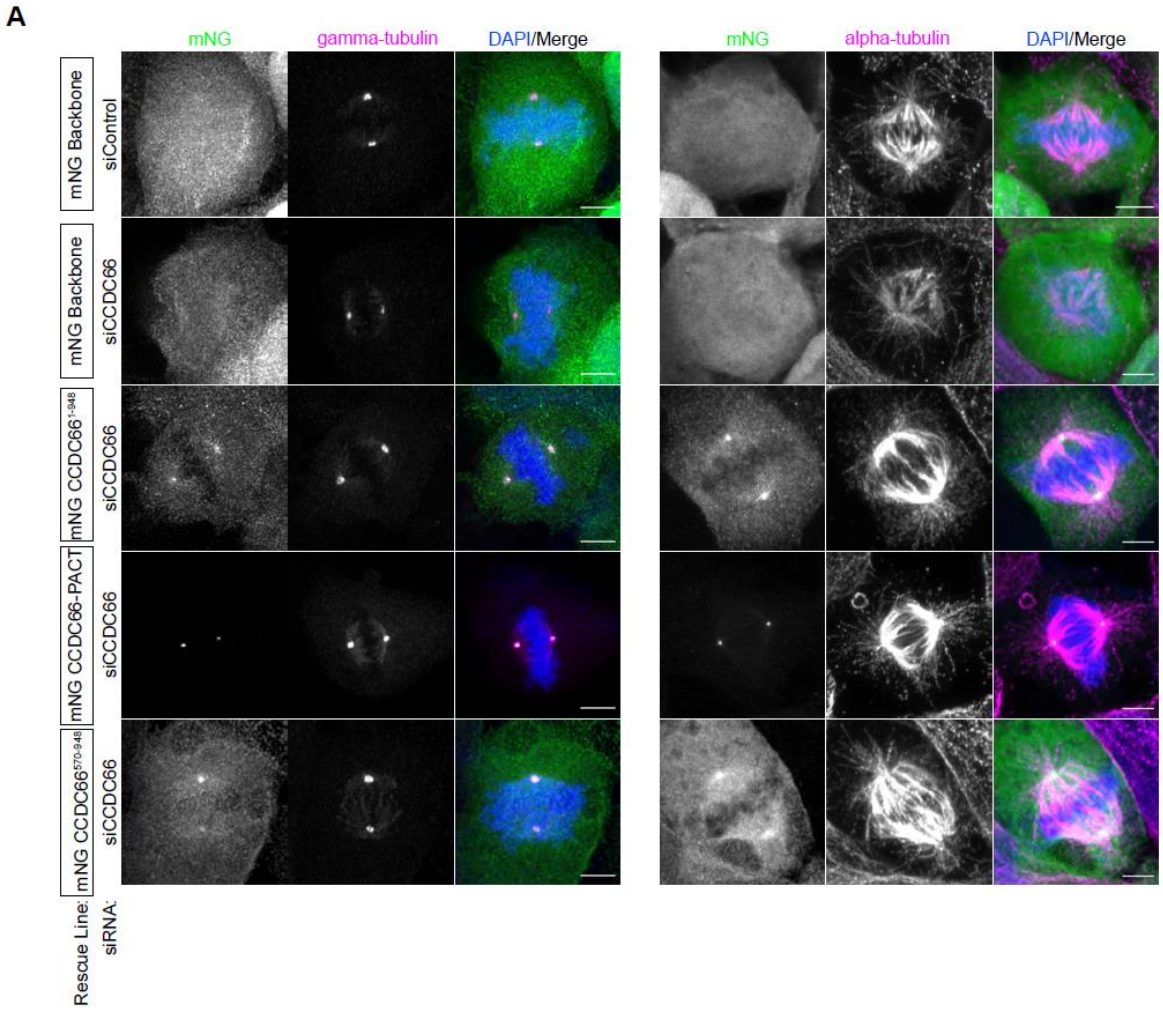

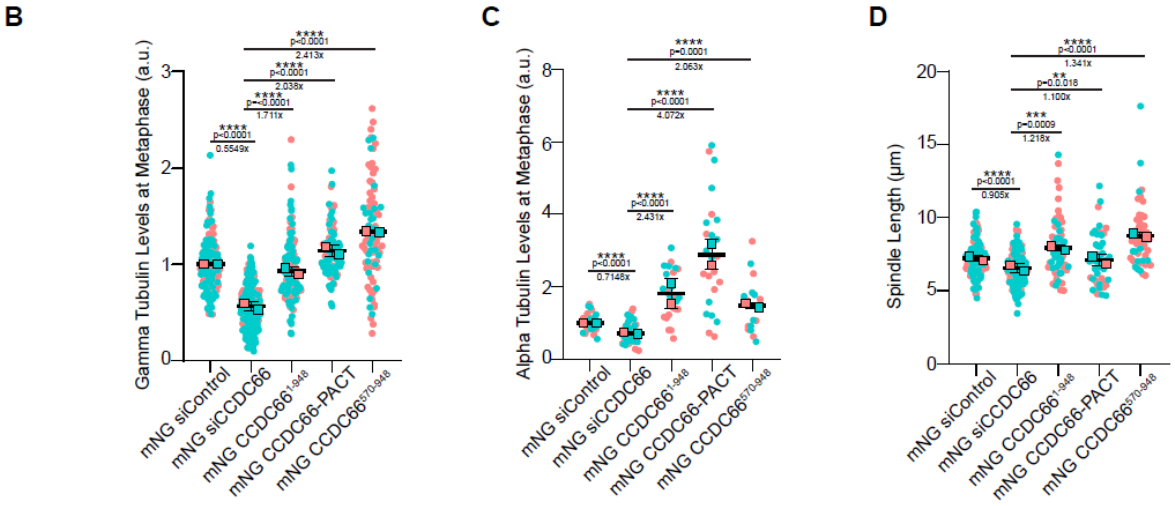

Figure 16. Centrosome and microtubule-affinity of CCDC66 is required for its mitotic functions

(A) Representative images for the rescue experiments performed using U2OS::mNeonGreen, U2OS::mNeonGreen-CCDC661-948, U2OS::mNeonGreen- CCDC66-PACT and U2OS::mNeonGreen-CCDC66570-948 stable cells. Cells were transfected with control and CCDC66 siRNA. 48 h post-transfection, they were fixed with 4% PFA and stained for either γ-tubulin or α-tubulin and DAPI. Scale bar: 5 µm. (B) Quantification of (A).gamma-tubulin intensity was measured on ImageJ by drawing a 3.4 µm2 circular area. Data represent the mean ±SEM of two independent experiments. (****p<0.0001)

(C) Quantification of (A). Spindle microtubule intensity was measured on ImageJ by taking several points on the spindle to measure the intensity then taking the average. Data represent the mean ±SEM of two independent experiments. (****p<0.0001).

(D) Quantification of (A). Spindle length is calculated by measuring the distance between two spindle poles. Data represent the mean ±SEM of two independent experiments. (**p<0.01 ***p<0.001 ****p<0.0001).

2.8 Materials and Methods

2.8.1 Plasmids

pDEST-GFP-CCDC66, pDEST-GFP-CCDC66RR and pDEST-Flag-CCDC66 plasmids used for transfection and transformation experiments were previously described (Conkar et al., 2017). Full-length CCDC66, CCDC66 (570-948) and CCDC66-PACT was

amplified by PCR and cloned into pCDH-EF1-mNeonGreen-T2A-Puro lentiviral expression plasmid. CCDC66 (570-948) was cloned into pDEST-His-MBP expression plasmid using Gateway cloning (Thermo Scientific). siRNA resistant mNG-CCDC66 was amplified from siRNA resistant GFP-CCDC66RR plasmid and cloned into pCDH-EF1- mNeonGreen-T2A-Puro plasmid. EB3-mNeonGreen-T2A-gamma-tubulin-tagRFP plasmid was a gift from Andrew Holland (Johns Hopkins University School of Medicine) (Yeow et al., 2020). Myc-BirA* fusions of CDK5RAP2, CEP192 and CEP152 and PLK1 were previously described. PLK1 was amplified by PCR and cloned into pDEST-Myc- BirA* plasmid using Gateway cloning. GFP-CEP55 plasmid was a gift from Kerstin Kutsche (UKE, Hamburg). GFP-PRC1 plasmid was a gift from Xuebiao Yao (Morehouse School of Medicine). mNeonGreen and mNeonGreen-CCDC66 were amplified by PCR and pDONR221 using Gateway recombination. Subsequent Gateway recombination reactions using pDEST-His-MBP (gift from David Waugh - Addgene plasmid # 11085) and pFastBac-DEST (gift from Tim Stearns; Gateway R1R2 destination cassette was cloned into pFastBac-HT-MBP-D using KpnI and XhoI) were performed to generate His- MBP-mNeonGreen and His-MBP-mNeonGreen-CCDC66 for expression for expression in bacterial cells and insect cells, respectively.

2.8.2 Cell culture and transfection

Human telomerase immortalized retinal pigment epithelium cells (hTERT-RPE1, ATCC, CRL-4000) were cultured with Dulbecco's modified Eagle's Medium DMEM/F12 50/50 medium (Pan Biotech,Cat. # P04-41250) supplemented with 10% Fetal Bovine Serum (FBS, Life Technologies, Ref. # 10270-106, Lot # 42Q5283K) and1% penicillin streptomycin (GIBCO, Cat. # 1540-122). Human embryonic kidney (HEK293T, ATCC, CRL-3216), and osteosarcoma epithelial (U2OS, ATCC, HTB-96) cells were cultured with DMEM medium (Pan Biotech, Cat. # P04-03590) supplemented with10% FBS and 1% penicillin-streptomycin. All cell lines were authenticated by Multiplex Cell Line Authentication (MCA) and were tested for mycoplasma by MycoAlert Mycoplasma Detection Kit (Lonza). U2OS cells were transfected with the plasmids using Lipofectamine 2000 and according to the manufacturer's instructions (Thermo Scientific Scientific). HEK293T cells were transfected with the plasmids using 1mg/ml polyethylenimine, MW 25 kDa (PEI). For microtubule depolymerization experiments, cells were treated with 5 µg/ml nocodazole (Sigma-Aldrich, Cat. #M1404) or vehicle (dimethyl sulfoxide) for one hour at 37 C. For cell synchronization experiments, 5 µM (+)-S-trityl-L-cysteine (STLC) (Alfa-Aesar, Cat. #2799-07-7) was used for 16 h at 37 C.

2.8.3 Lentivirus production and cell transduction

Lentivirus were generated using pcDH-mNG-CCDC66, pcDH-mNG-CCDC66 (570-948), pcDH-mNG-CCDC66-PACT and pCDH-EF1-mNeonGreen-T2A-Puro, and pLVPT2-mCherry-H2B plasmids as transfer vectors. For infection, 1 x 105 U2OS cells were seeded on 6-well tissue culture plates the day before infection, which were infected with 1 mL of viral supernatant the following day. 48-hour post-infection, cells were split and selected in the presence of 6mg/ml puromycin for RPE1s and 4mg/ml puromycin for U2OS cells for four to six days until all the control cells died. U2OS and RPE1 cells stably expressing mCherry-H2B and mNeonGreen fusions of full-length CCDC66 and its truncations were generated by infection of cells with lentivirus expressing the fusions.

2.8.4 siRNA and rescue experiments

CCDC66 was depleted using an siRNA with the sequence 5′-CAGTGTAATCAGTTCACAAtt-3′. Silencer Select Negative Control No. 1 (Thermo Scientific) was used as a control (Conkar et al., 2017). siRNAs were transfected into U2OS cells with Lipofectamine RNAiMax according to the manufacturer's instructions (Thermo Scientific Scientific). For rescue experiments, U2OS cells stably expressing mNG or mNG–CCDC66, mNG-CCDC66 PACT and mNG-CCDC66 570-948 were transfected with control and CCDC66 siRNAs by using Lipofectamine RNAiMax (Thermo Scientific Scientific). 48 h post transfection with the siRNAs, cells were fixed and stained.

2.8.5 Protein expression and purification

Protein expression in Rosetta (BL21(DE3)) cells transformed with respective constructs was induced by addition of 0.5 mM IPTG at OD600 of 0.5–0.6 for 16 hr at 18°C. BEVS baculovirus expression system and protocol (Fitzgerald et al., 2006) was used for expression of tagged full length CCDC66 protein. Briefly, 100 mL of Hi5 cells (1 x 106 cell/mL) were infected with P1 baculovirus produced in Sf9 cells, carrying His-MBPmNeonGreen- CCDC66, at MOI of 1. Cells were collected 48 hr after infection.

For protein purification, cells were lysed by sonication in lysis buffer (20 mM Hepes, pH 7.0 (or pH 7.5 for full length protein), 250 mM NaCl, 0.1% Tween20, 2 mg/ml lysozyme, 1 mM PMSF, 1mM protease inhibitor cocktail, 5mM BME and 10 mM Imidazole) and clarified at 19,000 rpm for 1 hr at 4°C. His-tagged proteins were subsequently purified using Ni-NTA–

agarose beads (Thermo Scientific). Proteins were eluted with elution buffer (20 mM Hepes, pH 7.0 or pH7.5, 250 mM NaCl, 5mM BME and 250 mM imidazole). For subsequent microtubule assays, proteins were dialyzed against BRB80 buffer (80 mM PIPES pH 6.8, 1 mM EGTA, 1m M MgCl2).

2.8.6 In Vitro MT bundling assay

Fluorescent MTs were polymerized at 2 mg/ml by incubating tubulin and rhodamine labeled tubulin (Cytoskeleton, Inc.) at 10:1 ratio in BRB80 with 1 mM DTT and 1mM GTP for 5 min on ice, then preclearing by centrifuging for 10 min at 90000 rpm at 2°C in TLA100 rotor. Cleared tubulin mixture was polymerized at 37°C by adding taxol and increasing concentration stepwise, with final concentration of 20 μM. MTs were pelleted over warm 40% glycerol BRB80 cushion at 70000 rpm for 20 min. After washes with 0.5% Triton-X100, pellet was resuspended in 80% of the starting volume of warm BRB80 buffer with 1mM DTT and 20 μM Taxol.

Bundling assays were performed as previously described (Tao et al., 2016). Briefly, 100 nM of protein His-MBP-CCDC66570-948, His-MBP-mNeonGreen, His-MBPmNeonGreen-CCDC66 or MBP was mixed with 2 μM MTs and 20 μM taxol in buffer T (20mM Tris, pH 8.0, 150mM KCl, 2mM MgCl2, 1mM DTT, protease inhibitors) for 30 min rocking at room temperature. The reaction mixtures were transferred into a flow chamber under a HCl-treated coverslip, and unstuck proteins were washed out with the excess of buffer T. Bundling of fluorescent MTs was observed with a Leica SP8 confocal microscope and 63x 1.4 NA oil objective (Leica Mycrosystems). Experiment was repeated 4 times.

2.8.7 In Vitro MT sedimentation assay

Purified bovine brain tubulin (Cytoskeleton Inc.) was precleared at 90000 rpm for 5 minutes at 2°C with TLA100 rotor. Cleared tubulin was polymerized at 1 mg/ml in the presence of 1 mM GTP and increasing concentrations of taxol to a final concentration of 20 μM. After incubation of microtubules at room temperature overnight, 500 nM of purified protein was mixed with 3 μM taxol-stabilized microtubules or BRB80 buffer with taxol and incubated for 30 minutes at room temperature. Samples were loaded onto 60% glycerol BRB80 cushions and centrifuged at 50000 rpm for 30 min with TLA100 rotor at room temperature. Supernatants

were collected, glycerol cushions removed by aspiration, and pellets solubilized in SDS sample buffer. Equivalent volumes of supernatant and pellet fractions were resolved by SDS-PAGE.

2.8.8 Ultra-Structure Expansion Microscopy (U-ExM)

U-ExM was performed as previously described (Gambarotto et al., 2019). Briefly, U2OS cells were transfected with siControl or siCCDC66. 48 hours after transfection, cells were treated with 5 μM STLC (Alfa-Aesar, Cat. #2799-07-7) for 16 h. Coverslips were incubated in 1.4% formaldehyde / 2% acrylamide (2X FA / AA) solution in 1X PBS for 5 h at 37 C prior to gelation in Monomer Solution supplemented with TEMED and APS (final concentration of 0.5%) for 1 hr at 37°C. Denaturation was performed at 95 C for 1h30 and gels were stained with primary antibodies for 3 h at 37 C. Gels were washed 3 X 10 min at RT with 1 X PBS with 0.1% Triton-X (PBST) prior to secondary antibody incubation for 2h30 at 37 C followed by 3 X 10 min washes in PBST at RT. Gels were expanded in 3 X 150 ml dH2O before imaging. The following reagents were used in U-ExM experiment: formaldehyde (FA, 36.5–38%, F8775, Sigma-Aldrich), acrylamide (AA, 40%, A4058, Sigma-Aldrich), N,N'-methylenbisacrylamide (BIS, 2%, M1533, SIGMA), sodium acrylate (SA, 97–99%, 408220, Sigma-Aldrich), ammonium persulfate (APS, 17874, Thermo Scientific), tetramethylethylendiamine (TEMED, 17919, Thermo Scientific), and poly-D-Lysine (A3890401, Gibco).

2.8.9 Immunofluorescence, antibodies, and microscopy

Cells were grown on coverslips, washed twice with PBS, and fixed in either ice cold methanol at 20 C for 10 minutes or 4% PFA in Cytoskeletal Buffer ((100 mM NaCl (Sigma-Aldrich, S9888), 300 mM sucrose (Sigma-Aldrich, S0389), 3 mM MgCl2 (Sigma-Aldrich, M2670), and 10 mM PIPES (Sigma-Aldrich, P6757). The pH of this solution was adjusted to 6.9. The final CB solution was filtered and stored at −20 °C until needed. CB was not used for more than 1 day after thawing. Immediately before use, for a 50 ml volume of CB, 250 μl of Triton X-100 and 250 μl of EGTA (1 M) (Sigma-Aldrich, E3889) were added.) for indirect immunofluorescence. After rehydration in PBS, cells were blocked with 3% BSA (Capricorn Scientific, Cat. # BSA-1T) in PBS followed by incubation with primary antibodies in blocking solution for 1 hour at room temperature. Cells were washed three times with PBS and incubated with secondary antibodies and DAPI (Thermo Scientific, cat#D1306) at1:2000 for 45 minutes

at room temperature. Following three washes with PBS, cells were mounted using Mowiol mounting medium containing N-propyl gallate (Sigma-Aldrich). Primary antibodies used for immunofluorescence were mouse anti-acetylated tubulin (clone 6-11B, 32270, Thermo Fischer) at 1:10000, mouse anti gamma-tubulin (Sigma, clone GTU-88, T5326) at 1:1000, rabbit anti GFP at 1:2000 (homemade), mouse anti alpha-tubulin (Sigma, DM1A) at 1:1000, rabbit anti CEP152 (Bethyl, A302-480A) at 1:500, rabbit anti-CEP192 (Proteintech, 18832 1 AP) at 1:1000, rabbit anti-phospho-Histone H3 at 1:1000, rabbit anti-CDK5RAP2 (Proteintech, 20061 1 AP) at 1:1000, rabbit anti-Pericentrin (Abcam, ab4448) at 1:2000, rabbit anti-CSPP1 (Proteintech, 11931 1 AP) at 1:1000, rabbit anti- PRC1 (Proteintech, 15617 1 AP) at 1:1000, rabbit anti-Cep55 (Proteintech, 23891 1 AP) at 1:1000, rabbit anti-Kif23 (Proteintech, 28587 1 AP), rabbit anti-pAurora A/B/C (Cell Signaling Technology, CST #2914) at 1:1000, and mouse anti-mNeonGreen (Chromotek, 32F6) at 1:500, rabbit anti-GFP was generated and used for immunofluorescence as previously described (Firat-Karalar et al., 2014; Hatch et al., 2010). Secondary antibodies used for immunofluorescence experiments were AlexaFluor 488-, 568- or 633-coupled (Life Technologies) and they were used at 1:2000.

Time lapse live imaging was performed with Leica SP8 confocal microscope equipped with an incubation chamber. For cell cycle experiments, asynchronous cells were imaged at 37C with 5% CO2 with a frequency of 6 minutes per frame with 1.5mm step size and 12mm stack size in 512x512 pixel format at a specific position using HC PL FLUOTAR 20x/0.50 DRY objective. For centrosomal protein level quantifications, images were acquired with Leica DMi8 inverted fluorescent microscope with a stack size of 8mm and step size of 0.3mm in 1024x1024 format using HC PL APO CS2 63x 1.4 NA oil objective. Higher resolution images were taken by using HC PL APO CS2 63x 1.4 NA oil objective with Leica SP8 confocal microscope.

Quantitative immunofluorescence for Cep192, Cep152, Cdk5Rap2, Pericentrin, gamma-Tubulin, PRC1 and Alpha-Tubulin was performed by acquiring a z stack of control and depleted cells using identical gain and exposure settings. The centrosome region for each cell were defined by staining for a centrosomal marker including gamma tubulin. The region of interest that encompassed the centrosome was defined as a circle 3.4-mm2 area centered on the centrosome in each cell. Total pixel intensity of fluorescence within the region of interest was measured using ImageJ (National Institutes of Health, Bethesda, MD). Background subtraction

was performed by quantifying fluorescence intensity of a region of equal dimensions in the area proximate to the centrosome. Statistical analysis was done by normalizing these values to their mean.

2.8.10 Spindle angle, length, and pole width measurements

U2OS cells were grown on coverslips and transfected with control and CCDC66 siRNA, fixed with methanol and stained for gamma-tubulin. Images are acquired with Leica DMi8 inverted fluorescence microscope at 1024x1024 format with 0.3 mm z step size. Spindle angle is calculated by the formula $\alpha=180*\tan\text{-}1(h/L)/\pi$ where h represents the z stack difference between two spindle poles, L represents the distance between spindle poles. Spindle length is calculated by measuring pole-to-pole distance. Spindle pole width is calculated by measuring the length of the pericentriolar material of the spindle pole as described in the illustrations in Fig. 4.

2.8.11 Quantitative analysis of the spindle and astral microtubule intensity

U2OS cells were grown on coverslips and transfected with control and CCDC66 siRNA, fixed with methanol and stained for alpha-tubulin. Images were acquired with Leica SP8 Confocal microscopy at 1024x1024 format with 2x zoom factor. For quantification of the astral microtubule intensity, 5 ROIs having XY size 2 microns were positioned manually on the astral microtubules and intensity was recorded. Background of the same ROI was measured in cytoplasm and subtracted from the average signal intensity. For astral microtubule length, the longest microtubule was measured using the length tool on ImageJ. For quantification of spindle microtubule intensity, 10 ROIs having XY size 2 microns were positioned manually on the spindle microtubules and intensity was recorded. Background of the same ROI was measured in cytoplasm and subtracted from the average signal intensity. For acetylated tubulin, cells were stained with acetylated tubulin and imaged with Leica DMi8 inverted fluorescence microscope. Like alpha tubulin intensity measurement, 10 ROIs having XY size 5 microns were positioned manually on the spindle microtubules and intensity was recorded. Background of the same ROI was measured in cytoplasm and subtracted from the average signal intensity. The values of control and CCDC66 siRNA-treated metaphase cells were plotted relative to mean intensity of control siRNA.

2.8.12 Microtubule regrowth assay

U2OS cells were grown on poly-L-lysine coated coverslips and treated with control or CCDC66 siRNA. After 48 h of transfection, cells were treated with 5 μM/ml STLC for 16h. Next day, cells were treated with 5 μg/ml nocodazole for 1 at 37 C. Cells were washed extensively with cold PBS to prevent MT polymerization then incubated with warm media and fixed at indicated time points and stained for alpha tubulin and gamma tubulin. Images were acquired with Leica SP8 Confocal microscopy at 1024x1024 format with 2x zoom factor. To quantify MT nucleation area, polygon selection tool on ImageJ is used. MT nucleation points were assessed based on tubulin staining.

2.8.13 Immunoprecipitation

HEK293T cells were co-transfected with indicated plasmids. 48 post-transfection, cells were washed and lysed with lysis buffer (50 mM HEPES pH 8, 100 mM KCl, 2 mM EDTA, 10% glycerol, 0.1 % NP-40, Protease inhibitors 1:100 pro-block PIC + 1:100 PMSF) for 45 min. Lysates were centrifuged at 13000 rpm for 10 min at 4°C, and supernatants were transferred to a tube. 100 μl from each sample was saved as input. The rest of the supernatant was immunoprecipitated with anti-FLAG M2 agarose beads (Sigma-Aldrich) over-night at 4°C. After washing 3X with lysis buffer, samples were resuspended in SDS containing sample buffer and analyzed by immunoblotting.

2.8.14 Cell lysis and immunoblotting

Cells were lysed in 50 mM Tris (pH 7.6), 150 mM NaCI, 1% Triton X-100 and protease inhibitors for 30 min at 4C followed by centrifugation at 15.000 g for 15 min. The protein concentration of the resulting supernatants was determined with the Bradford solution (Bio-Rad Laboratories, CA, USA). For immunoblotting, equal quantities of cell extracts were resolved on SDS-PAGE gels, transferred onto nitrocellulose membranes, blocked with TBST in 5% milk for 1 hour at room temperature. Blots were incubated with primary antibodies diluted in 5% BSA in TBST overnight at 4C, washed with TBST three times for 5 minutes and blotted with secondary antibodies for 1 hour at room temperature. After washing blots with TBST three times for 5 minutes, they were visualized with the LI-COR Odyssey® Infrared Imaging System and software at 169 mm (LI-COR Biosciences). Primary antibodies used for immunofluorescence were mouse anti acetylated tubulin (clone 6-11B, 32270, Thermo Fischer) at 1:10000, mouse anti gamma-tubulin (Sigma, clone GTU-88, T5326) at 1:5000, rabbit anti

GFP at 1:10000 (homemade), mouse anti alpha-tubulin (Sigma, DM1A) at 1:5000, rabbit anti CEP152 (Bethyl, A302-480A) at 1:1000, rabbit anti-CEP192 (Proteintech, 18832 1 AP) at 1:1000, rabbit anti-Cdk5Rap2 (Proteintech, 20061 1 AP) at 1:1000, rabbit anti-Pericentrin (Abcam, ab4448) at 1:2000, mouse anti-mNG (Chromotek, 32F6) and mouse anti- CCDC66 (sigma SAB1408484) at 1:500. Secondary antibodies used for western blotting experiments were IRDye680- and IRDye800-coupled and were used at 1:15000 (LICOR Biosciences). Secondary antibodies used for western blotting experiments were IRDye680- and IRDye800-coupled and were used at 1:15000 (LI-COR Biosciences).

2.8.15 Quantification and statistical analysis

Data were analyzed and plotted using GrapPad Prism 7 (GraphPad, La Jolla, CA). Results are shown as mean ± standard errors (SEM) of the mean. Number of biological replicates are indicated in the figure legends. Two-tailed unpaired t tests and one-way analysis of variance (ANOVA) were applied to compare the statistical significance of the measurements. Error bars reflect SD. Following key is followed for asterisk place holders for p-values in the figures: *$p < 0.05$, **$p < 0.01$, ***$p < 0.001$, **** $p < 0.0001$ ns. not significant

Chapter 3:
DISCUSSION

In this study, we identified the centrosomal and ciliary MAP, CCDC66, as a new player of the machinery governing the assembly and organization of the mitotic and cytokinetic MT arrays and thereby cell cycle progression. Our findings reveal two important roles of CCDC66 during cell division. First, CCDC66 is required for mitotic progression via regulation of spindle assembly, organization and positioning, levels of spindle MTs, kfiber integrity and chromosome congression. Second, CCDC66 functions during cytokinesis in part by regulating organization of central spindle and midbody MTs. Our work provides new insights into the spatiotemporal regulation of the mitotic and cytokinetic events governed by drastic changes of the MT cytoskeleton and centrosomes.

The results of our study reveal two major mechanisms by which CCDC66 functions during cell cycle progression. First, it regulates centrosome maturation via recruitment of core PCM proteins and is required for MT nucleation during bipolar spindle assembly. While its function during centrosome maturation identifies CCDC66 as a regulator of centrosome-mediated MT nucleation, it is likely that CCDC66 is also a component of the machinery for MT-mediated MT nucleation during spindle assembly. The latter mechanism is supported by the proximity interactions of CCDC66 with all 8 subunits of the HAUS/Augmin complex, which recruits γ-TuRC to MTs and promotes nucleation from spindle MTs (Gheiratmand et al., 2019). Future studies are required to investigate whether and if so how CCDC66 regulates HAUS complex-dependent MT nucleation. Interestingly, CCDC66 also directly interacts with gamma-tubulin apart from binding to alpha and beta-tubulin. It will be worthwhile to characterize in vitro direct contribution of CCDC66 on gamma and alpha/beta-tubulin recruitment and de novo MT formation.

The second mechanism by which CCDC66 operates during mitosis is organization of MTs via its crosslinking activity. Stabilization and bundling of MTs is essential for the assembly and maintenance of the MT arrays of cell division such as the k-fibers, central spindle and midbody. In CCDC66-depleted cells, MTs at the central spindle and midbody were disorganized as compared to the thick and aligned bundles of control cells. CCDC66 loss also

interferes with k-fiber integrity. While our findings define CCDC66 as a new player of MT crosslinking during cell division, they also raise several important questions that pertain to the mechanisms by which CCDC66 crosslinks MTs, whether CCDC66 selectively bundles parallel or anti-parallel bundles and whether CCDC66 cooperate or compete with other crosslinking proteins. Notably, CCDC66 interacts and co-localizes with PRC1, one of the best characterized MAPs involved in organization of MTs during cell division. PRC1-mediated MT crosslinking and protein recruitment at the bridging fibers and central spindle were shown to be required for chromosome alignment and successful completion of cytokinesis, respectively (Jagric et al., 2021; Jiang et al., 1998; Mollinari et al., 2002; Subramanian et al., 2010; Tolic, 2018; Zhu and Jiang, 2005). Future studies utilizing spatial and temporal depletion of CCDC66 in cells will reveal whether and if so how CCDC66 regulates these processes and contribute to our understanding of the precise functions and mechanisms of CCDC66 at different stages of the cell cycle. For example, the mitotic functions of PRC1 during chromosome alignment was revealed using an optogenetic-based mislocalization approach. This study also showed that acute removal of PRC1 from the spindle by optogenetics and its long-term depletion by siRNA led to partially different phenotypes, likely due to the compensatory mechanisms that mask phenotypes during long-term depletion.

Spindle positioning is critical for specification of the site of the cleavage furrow and distribution of cell fate determinants to daughter cells during tissue architecture and organization (Kotak, 2019; Kotak and Gonczy, 2013). Accordingly, its deregulation is implicated in developmental disorders affecting organs such as the kidney and brain. Importantly, we found that CCDC66 is required for proper spindle positioning via regulating astral MT density and length. We also note that astral MTs cooperate with the dynein complex to position the spindle. During metaphase, cytoplasmic dynein is enriched at the cell cortex, where it exerts pulling forces on the plus ends of astral MTs (Kiyomitsu and Cheeseman, 2012; Kotak, 2019; Kotak and Gonczy, 2013). In previous work, the dynactin complex subunit p150glued and dynein complex subunit DYNC1IC1 were identified as CCDC66 cellular interactors (Conkar et al., 2019; Redwine et al., 2017). Therefore, regulation of p150glued localization and function by CCDC66 could be another potential mechanism by which CCDC66 regulates spindle positioning.

While its roles in MT nucleation explains defects in spindle MT levels and positioning, the mechanisms that underlie the astral and spindle MT length defects in CCDC66-depleted cells are not completely understood and needs further investigation. We envision several different mechanisms. Spatiotemporal regulation of MT polymerization, sliding and depolymerization is critical to spindle length maintenance (Dumont and Mitchison, 2009). CCDC66 localization on these MT sub-types could suggest direct effect on their dynamics, stability, and length. Alternatively, length phenotypes could be attributed to regulation of other regulators of MT stability and dynamics by CCDC66. Further analysis of CCDC66 interaction with those regulators of MT dynamics and stability that are revealed with high throughput proximity-mapping studies, identification of the CCDC66 mitotic interactome as well as future in vitro MT reconstitution assays, will contribute to better understanding of spindle dynamics regulation by CCDC66.

The remarkably dynamic localization of CCDC66 to different cellular compartments during mitosis makes it challenging to define whether its functions during cell division are mediated by its specific pools or requires their coordinated activity. To address these questions, we performed phenotypic rescue experiments with CCDC66 truncation mutants. Strikingly, forced localization of CCDC66 at the centrosome was sufficient to rescue reduced spindle length and MT density and defective gamma-tubulin targeting to the spindle poles. This result suggests that centrosomal CCDC66 might be sufficient for these functions. However, it also does not exclude the contribution of the MT-associated CCDC66 pools to these processes for two potential reasons we envision. First, full length CCDC66 and its C-terminal domain rescued these phenotypes to a greater extent than CCDC66-PACT, suggesting that centrosomal and MT pools might cooperate in these processes. Second, the strong centrosome affinity of the PACT domain used to restrict CCDC66 localization at the centrosome increased the its centrosomal levels and likely created more binding sites for its interactors such as gamma-tubulin. These changes in centrosomal levels of gamma-tubulin and likely other proteins might compensate for its MT-associated functions. To distinguish between these possibilities and to address specific functions of the MT-pool of CCDC66, precise understanding of the mechanism by which it interacts with MTs is required. Knowledge about the structure of CCDC66-MT interaction surface will inform generation of new tools for phenotypic rescue experiments such as CCDC66 MT-binding mutants.

CCDC66 has been implicated in several developmental disorders. Frameshift mutations in dogs and its deletion in mouse cause retinal degeneration (Dekomien et al., 2010; Gerding et al., 2011; Murgiano et al., 2020; Schreiber et al., 2018). Additionally, CCDC66 was reported to interact with proteins mutated Joubert syndrome, suggesting putative functions for CCDC66 during neurogenesis (Latour et al., 2020). Although these mutations phenotypes can be explained by CCDC66 functions at the primary cilium, we cannot exclude the potential contribution of its non-ciliary functions to these reported developmental defects or uncharacterized ones. We note that CCDC66-/- mice was only characterized for developmental defects affecting retina and olfactory bulb, but not for the ones associated with misoriented cell division such as cystogenesis (Fischer et al., 2006). Finally, CCDC66-/- mice were embryonically viable and did not develop tumors, indicating that defective cell cycle defects linked to CCDC66 loss alone do not disrupt embryogenesis and is not tumorigenic (Gerding et al., 2011). This might be due to the compensatory mechanisms activated upon chronic loss of CCDC66, which is supported by its evolutionary conservation profile. CCDC66 is not as highly conserved as the HAUS complex or the core PCM proteins that it interacts with, suggesting that it is not an essential conserved player of cell division but instead vertebrate-specific regulatory protein required for regulating the fidelity of cell division. Future studies using spatially and temporally controlled in vivo experiments are required to determine whether nonciliary functions of CCDC66 contribute to developmental disorders.

BIBLIOGRAPHY

Akhmanova, A., C.C. Hoogenraad, K. Drabek, T. Stepanova, B. Dortland, T. Verkerk, W. Vermeulen, B.M. Burgering, C.I. De Zeeuw, F. Grosveld, and N. Galjart. 2001. Clasps are CLIP-115 and -170 associating proteins involved in the regional regulation of microtubule dynamics in motile fibroblasts. *Cell.* 104:923-935.

Akhmanova, A., and M.O. Steinmetz. 2015. Control of microtubule organization and dynamics: two ends in the limelight. Nat Rev Mol Cell Biol. 16:711-726. Booth, D.G., F.E. Hood, I.A. Prior, and S.J. Royle. 2011. A TACC3/ch-TOG/clathrin complex stabilises kinetochore fibres by inter-microtubule bridging. *EMBO J.* 30:906-919.

Cabral, G., T. Laos, J. Dumont, and A. Dammermann. 2019. Differential Requirements for Centrioles in Mitotic Centrosome Growth and Maintenance. Dev Cell. 50:355- 366 e356. Choi, Y.K., P. Liu, S.K. Sze, C. Dai, and R.Z. Qi. 2010. CDK5RAP2 stimulates microtubule nucleation by the gamma-tubulin ring complex. *J Cell Biol.* 191:1089- 1095.

Conduit, P.T., Z. Feng, J.H. Richens, J. Baumbach, A. Wainman, S.D. Bakshi, J. Dobbelaere, S. Johnson, S.M. Lea, and J.W. Raff. 2014. The centrosome-specific phosphorylation of Cnn by Polo/Plk1 drives Cnn scaffold assembly and centrosome maturation. *Dev Cell.* 28:659-669.

Conkar, D., H. Bayraktar, and E.N. Firat-Karalar. 2019. Centrosomal and ciliary targeting of CCDC66 requires cooperative action of centriolar satellites, microtubules, and molecular motors. *Sci Rep.* 9:14250.

Conkar, D., E. Culfa, E. Odabasi, N. Rauniyar, J.R. Yates, 3rd, and E.N. Firat-Karalar. 2017. Centriolar satellite protein CCDC66 interacts with CEP290 and functions in cilium formation and trafficking. *J Cell Sci*.

Dekomien, G., C. Vollrath, E. Petrasch-Parwez, M.H. Boeve, D.A. Akkad, W.M. Gerding, and J.T. Epplen. 2010. Progressive retinal atrophy in Schapendoes dogs: mutation of the newly identified CCDC66 gene. *Neurogenetics.* 11:163-174.

Delaval, B., A. Bright, N.D. Lawson, and S. Doxsey. 2011. The cilia protein IFT88 is required for spindle orientation in mitosis. *Nat Cell Biol.* 13:461-468.

Dobbelaere, J., F. Josue, S. Suijkerbuijk, B. Baum, N. Tapon, and J. Raff. 2008. A genome-wide RNAi screen to dissect centriole duplication and centrosome maturation in Drosophila. *PLoS Biol*. 6:e224.

Fischer, E., E. Legue, A. Doyen, F. Nato, J.F. Nicolas, V. Torres, M. Yaniv, and M. Pontoglio. 2006. Defective planar cell polarity in polycystic kidney disease. *Nat Genet.* 38:21-23.

Fry, A.M., J. Sampson, C. Shak, and S. Shackleton. 2017. Recent advances in pericentriolar material organization: ordered layers and scaffolding gels. *F1000Res.* 6:1622.

Gambarotto, D., F.U. Zwettler, M. Le Guennec, M. Schmidt-Cernohorska, D. Fortun, S. Borgers, J. Heine, J.G. Schloetel, M. Reuss, M. Unser, E.S. Boyden, M. Sauer, V. Hamel, and P. Guichard. 2019. Imaging cellular ultrastructures using expansion microscopy (U-ExM). *Nat Methods.* 16:71-74.

Gerding, W.M., S. Schreiber, T. Schulte-Middelmann, A. de Castro Marques, J. Atorf, D.A. Akkad, G. Dekomien, J. Kremers, R. Dermietzel, A. Gal, T. Rulicke, S. Ibrahim, J.T. Epplen, and E. Petrasch-Parwez. 2011. Ccdc66 null mutation causes retinal degeneration and dysfunction. *Hum Mol Genet.* 20:3620-3631.

Gheiratmand, L., E. Coyaud, G.D. Gupta, E.M. Laurent, M. Hasegan, S.L. Prosser, J. Goncalves, B. Raught, and L. Pelletier. 2019. Spatial and proteomic profiling reveals centrosome-independent features of centriolar satellites. *EMBO J.*

Glotzer, M. 2009. The 3Ms of central spindle assembly: microtubules, motors and MAPs. *Nat Rev Mol Cell Biol.* 10:9-20.

Gomez-Ferreria, M.A., U. Rath, D.W. Buster, S.K. Chanda, J.S. Caldwell, D.R. Rines, and D.J. Sharp. 2007. Human Cep192 is required for mitotic centrosome and spindle assembly. *Curr Biol.* 17:1960-1966.

Goshima, G., M. Mayer, N. Zhang, N. Stuurman, and R.D. Vale. 2008. Augmin: a protein complex required for centrosome-independent microtubule generation within the spindle. *J Cell Biol.* 181:421-429.

Goshima, G., R. Wollman, S.S. Goodwin, N. Zhang, J.M. Scholey, R.D. Vale, and N. Stuurman. 2007. Genes required for mitotic spindle assembly in Drosophila S2 cells. *Science*. 316:417-421.

Green, R.A., and K.B. Kaplan. 2003. Chromosome instability in colorectal tumor cells is associated with defects in microtubule plus-end attachments caused by a dominant mutation in APC. *J Cell Biol.* 163:949-961.

Gupta, G.D., E. Coyaud, J. Goncalves, B.A. Mojarad, Y. Liu, Q. Wu, L. Gheira Comartin, J.M. Tkach, S.W. Cheung, M. Bashkurov, M. Hasegan, J.D. Knight, Z.Y. Lin, M. Schueler, F. Hildebrandt, J. Moffat, A.C. Gingras, B. Raught, and L. Pelletier. 2015. A Dynamic Protein Interaction Landscape of the Human Centrosome-Cilium Interface. *Cell.* 163:1484-1499.

Hanafusa, H., S. Kedashiro, M. Tezuka, M. Funatsu, S. Usami, F. Toyoshima, and K. Matsumoto. 2015. PLK1-dependent activation of LRRK1 regulates spindle orientation by phosphorylating CDK5RAP2. *Nat Cell Biol.* 17:1024-1035.

Heald, R., R. Tournebize, T. Blank, R. Sandaltzopoulos, P. Becker, A. Hyman, and E. Karsenti. 1996. Self-organization of microtubules into bipolar spindles around artificial chromosomes in Xenopus egg extracts. *Nature*. 382:420-425.

Hu, C.K., M. Coughlin, and T.J. Mitchison. 2012. Midbody assembly and its regulation during cytokinesis. *Mol Biol Cell*. 23:1024-1034.

Huhn, S.C., J. Liu, C. Ye, H. Lu, X. Jiang, X. Feng, S. Ganesan, E. White, and Z. Shen. 2017. Regulation of spindle integrity and mitotic fidelity by BCCIP. *Oncogene*. 36:4750-4766.

Jagric, M., P. Risteski, J. Martincic, A. Milas, and I.M. Tolic. 2021. Optogenetic control of PRC1 reveals its role in chromosome alignment on the spindle by overlap lengthdependent forces. *eLife*. 10.

Jiang, W., G. Jimenez, N.J. Wells, T.J. Hope, G.M. Wahl, T. Hunter, and R. Fukunaga. 1998. PRC1: a human mitotic spindle-associated CDK substrate protein required for cytokinesis. *Mol Cell*. 2:877-885.

Joukov, V., J.C. Walter, and A. De Nicolo. 2014. The Cep192-organized aurora A-Plk1 cascade is essential for centrosome cycle and bipolar spindle assembly. *Mol Cell.* 55:578-591.

Kaplan, K.B., A.A. Burds, J.R. Swedlow, S.S. Bekir, P.K. Sorger, and I.S. Nathke. 2001. A role for the Adenomatous Polyposis Coli protein in chromosome segregation. *Nat Cell Biol*. 3:429-432.

Kiyomitsu, T., and I.M. Cheeseman. 2012. Chromosome- and spindle-pole-derived signals generate an intrinsic code for spindle position and orientation. *Nat Cell Biol*. 14:311-317.

Kotak, S. 2019. Mechanisms of Spindle Positioning: Lessons from Worms and Mammalian Cells. *Biomolecules*. 9.

Kotak, S., and P. Gonczy. 2013. Mechanisms of spindle positioning: cortical force generators in the limelight. *Curr Opin Cell Biol*. 25:741-748.

Latour, B.L., J.C. Van De Weghe, T.D. Rusterholz, S.J. Letteboer, A. Gomez, R. Shaheen, M. Gesemann, A. Karamzade, M. Asadollahi, M. Barroso-Gil, M. Chitre, M.E. Grout, J. van Reeuwijk, S.E. van Beersum, C.V. Miller, J.C. Dempsey, H. Morsy, M.J. Bamshad, D.A. Nickerson, S.C. Neuhauss, K. Boldt, M. Ueffing, M. Keramatipour, J.A. Sayer, F.S. Alkuraya, R. Bachmann-Gagescu, R. Roepman, and D. Doherty. 2020. Dysfunction of the ciliary ARMC9/TOGARAM1 protein module causes Joubert syndrome. *J Clin Invest*.

Lee, K., and K. Rhee. 2011. PLK1 phosphorylation of pericentrin initiates centrosome maturation at the onset of mitosis. *J Cell Biol*. 195:1093-1101.

Luders, J. 2012. The amorphous pericentriolar cloud takes shape. *Nat Cell Biol*. 14:1126-1128.

McDonald, K.L., E.T. O'Toole, D.N. Mastronarde, and J.R. McIntosh. 1992. Kinetochore microtubules in PTK cells. *J Cell Biol.* 118:369-383.

McEwen, B.F., A.B. Heagle, G.O. Cassels, K.F. Buttle, and C.L. Rieder. 1997. Kinetochore fiber maturation in PtK1 cells and its implications for the mechanisms of chromosome congression and anaphase onset. *J Cell Biol.* 137:1567-1580.

McKinley, K.L., and I.M. Cheeseman. 2017. Large-Scale Analysis of CRISPR/Cas9 Cell-Cycle Knockouts Reveals the Diversity of p53-Dependent Responses to Cell- Cycle Defects. *Dev Cell.* 40:405-420 e402.

Mollinari, C., J.P. Kleman, W. Jiang, G. Schoehn, T. Hunter, and R.L. Margolis. 2002. PRC1 is a microtubule binding and bundling protein essential to maintain the mitotic spindle midzone. *J Cell Biol*. 157:1175-1186.

Murgiano, L., D. Becker, C. Spector, K. Carlin, E. Santana, J.K. Niggel, V. Jagannathan, T. Leeb, S. Pearce-Kelling, G.D. Aguirre, and K. Miyadera. 2020. CCDC66 frameshift variant associated with a new form of early-onset progressive retinal atrophy in Portuguese Water Dogs. *Sci Rep.* 10:21162.

Palazzo, R.E., J.M. Vogel, B.J. Schnackenberg, D.R. Hull, and X. Wu. 2000. Centrosome maturation. *Curr Top Dev Biol*. 49:449-470.

Petry, S. 2016. Mechanisms of Mitotic Spindle Assembly. *Annu Rev Biochem*. 85:659- 683.

Petry, S., and R.D. Vale. 2015. Microtubule nucleation at the centrosome and beyond. *Nat Cell Biol.* 17:1089-1093.

Redwine, W.B., M.E. DeSantis, I. Hollyer, Z.M. Htet, P.T. Tran, S.K. Swanson, L. Florens, M.P. Washburn, and S.L. Reck-Peterson. 2017. The human cytoplasmic dynein interactome reveals novel activators of motility. *eLife*. 6.

Schreiber, S., E. Petrasch-Parwez, E. Porrmann-Kelterbaum, E. Forster, J.T. Epplen, and W.M. Gerding. 2018. Neurodegeneration in the olfactory bulb and olfactory deficits in the Ccdc66 -/- mouse model for retinal degeneration. *IBRO Rep*. 5:43- 53.

Shaner, N.C., G.G. Lambert, A. Chammas, Y. Ni, P.J. Cranfill, M.A. Baird, B.R. Sell, J.R. Allen, R.N. Day, M. Israelsson, M.W. Davidson, and J. Wang. 2013. A bright monomeric green fluorescent protein derived from Branchiostoma lanceolatum. *Nat Methods*. 10:407-409.

Sharp, J.A., J.J. Plant, T.K. Ohsumi, M. Borowsky, and M.D. Blower. 2011. Functional analysis of the microtubule-interacting transcriptome. *Mol Biol Cell*. 22:4312- 4323.

Subramanian, R., E.M. Wilson-Kubalek, C.P. Arthur, M.J. Bick, E.A. Campbell, S.A. Darst, R.A. Milligan, and T.M. Kapoor. 2010. Insights into antiparallel microtubule crosslinking by PRC1, a conserved nonmotor microtubule binding protein. *Cell.* 142:433-443.

Syred, H.M., J. Welburn, J. Rappsilber, and H. Ohkura. 2013. Cell cycle regulation of microtubule interactomes: multi-layered regulation is critical for the interphase/mitosis transition. *Mol Cell Proteomics*. 12:3135-3147.

Tao, L., B. Fasulo, B. Warecki, and W. Sullivan. 2016. Tum/RacGAP functions as a switch activating the Pav/kinesin-6 motor. *Nat Commun.* 7:11182.

Taulet, N., A. Douanier, B. Vitre, C. Anguille, J. Maurin, Y. Dromard, V. Georget, and B. Delaval. 2019. IFT88 controls NuMA enrichment at k-fibers minus-ends to facilitate their re-anchoring into mitotic spindles. *Sci Rep.* 9:10311.

Tolic, I.M. 2018. Mitotic spindle: kinetochore fibers hold on tight to interpolar bundles. *Eur Biophys J.* 47:191-203.

Villari, G., C. Enrico Bena, M. Del Giudice, N. Gioelli, C. Sandri, C. Camillo, A. Fiorio Pla, C. Bosia, and G. Serini. 2020. Distinct retrograde microtubule motor sets drive early and late endosome transport. *EMBO J*. 39:e103661.

Vukusic, K., R. Buda, A. Bosilj, A. Milas, N. Pavin, and I.M. Tolic. 2017. Microtubule Sliding within the Bridging Fiber Pushes Kinetochore Fibers Apart to Segregate Chromosomes. *Dev Cell*. 43:11-23 e16.

Yeow, Z.Y., B.G. Lambrus, R. Marlow, K.H. Zhan, M.A. Durin, L.T. Evans, P.M. Scott, T. Phan, E. Park, L.A. Ruiz, D. Moralli, E.G. Knight, L.M. Badder, D. Novo, S. Haider, C.M. Green, A.N.J. Tutt, C.J. Lord, J.R. Chapman, and A.J. Holland. 2020. Targeting TRIM37-driven centrosome dysfunction in 17q23-amplified breast cancer. *Nature*. 585:447-452.

Zhu, C., and W. Jiang. 2005. Cell cycle-dependent translocation of PRC1 on the spindle by Kif4 is essential for midzone formation and cytokinesis. *Proc Natl Acad Sci U S A.* 102:343-348.